Geosci. Model Dev., 7, 361–386, 2014
www.geosci-model-dev.net/7/361/2014/
doi:10.5194/gmd-7-361-2014

Geoscientific Model Development
Open Access

The Met Office Unified Model Global Atmosphere 4.0 and JULES Global Land 4.0 configurations

D. N. Walters[1], K. D. Williams[1], I. A. Boutle[1], A. C. Bushell[1], J. M. Edwards[1], P. R. Field[1], A. P. Lock[1], C. J. Morcrette[1], R. A. Stratton[1], J. M. Wilkinson[1], M. R. Willett[1], N. Bellouin[1,2], A. Bodas-Salcedo[1], M. E. Brooks[1], D. Copsey[1], P. D. Earnshaw[1], S. C. Hardiman[1], C. M. Harris[1], R. C. Levine[1], C. MacLachlan[1], J. C. Manners[1], G. M. Martin[1], S. F. Milton[1], M. D. Palmer[1], M. J. Roberts[1], J. M. Rodríguez[1], W. J. Tennant[1], and P. L. Vidale[3]

[1]Met Office, FitzRoy Road, Exeter, EX1 3PB, UK
[2]Department of Meteorology, University of Reading, Reading, RG6 6BB, UK
[3]National Centre for Atmospheric Science, Department of Meteorology, University of Reading, Reading, RG6 6BB, UK

Correspondence to: D. N. Walters (david.walters@metoffice.gov.uk)

Received: 1 March 2013 – Published in Geosci. Model Dev. Discuss.: 14 May 2013
Revised: 8 January 2014 – Accepted: 8 January 2014 – Published: 20 February 2014

Abstract. We describe Global Atmosphere 4.0 (GA4.0) and Global Land 4.0 (GL4.0): configurations of the Met Office Unified Model and JULES (Joint UK Land Environment Simulator) community land surface model developed for use in global and regional climate research and weather prediction activities. GA4.0 and GL4.0 are based on the previous GA3.0 and GL3.0 configurations, with the inclusion of developments made by the Met Office and its collaborators during its annual development cycle.

This paper provides a comprehensive technical and scientific description of GA4.0 and GL4.0 as well as details of how these differ from their predecessors. We also present the results of some initial evaluations of their performance. Overall, performance is comparable with that of GA3.0/GL3.0; the updated configurations include improvements to the science of several parametrisation schemes, however, and will form a baseline for further ongoing development.

1 Introduction

For more than twenty years, the Met Office has used a single atmospheric model, the Met Office Unified Model™ (MetUM), for its global and regional Numerical Weather Prediction (NWP) and climate research activities (Cullen, 1993). The MetUM's land surface scheme (Cox et al., 1999), and more recently the JULES (Joint UK Land Environment Simulator; Best et al., 2011; Clark et al., 2011) community land surface model, has allowed us to do the same in modelling the land surface and surface exchange processes. This provides the technical efficiency of sharing a common code infrastructure and libraries of parametrisations, and allows us to take scientific advantage of the recognised synergies between climate and NWP modelling (e.g. Martin et al., 2010; Senior et al., 2010). By studying the same model formulation across a range of timescales and system applications, one can learn about the rate of growth and nature of both model errors and desirable behaviours. Also, by constraining configurations to perform adequately across a wide variety of systems, scientists can be more confident that model developments seen to improve performance metrics in any one system are doing so by modelling a truer representation of the real atmosphere.

It is for this reason that the Met Office is attempting to adopt a single set of atmospheric and land surface model configurations for use in global and regional models across timescales from short-range weather prediction to multi-centennial climate projections: the MetUM Global Atmosphere and JULES Global Land. The principle of the Global Atmosphere and Global Land development processes and the justification of this approach were described in detail in Walters et al. (2011). An important part of this is the publication of a paper describing each release developed over an annual cycle; the current paper and the developments described herein present a first attempt to apply these principles

in practice in the development of the Global Atmosphere 4.0 (GA4.0) and Global Land 4.0 (GL4.0) configurations.

In Sect. 2 we provide a description of GA4.0 and GL4.0[1,2], whilst in Sect. 3 we describe the main enhancements made since GA3.0/GL3.0 in more detail. Section 4 provides a preliminary evaluation of the performance of the configuration in several systems. Finally, Sect. 5 includes some lessons learnt over the course of the development cycle and outlines our priorities for future development.

2 Global Atmosphere 4.0 and Global Land 4.0

2.1 Dynamical formulation and discretisation

The MetUM's dynamical core uses a semi-implicit semi-Lagrangian formulation to solve the non-hydrostatic, fully compressible deep-atmosphere equations of motion (Davies et al., 2005). The primary dry atmospheric prognostics are the three-dimensional wind components, potential temperature, Exner pressure, and density, whilst moist prognostics such as the mass mixing ratio of water vapour and prognostic cloud fields are advected as free tracers; the same is also true of other atmospheric loadings. These prognostic fields are discretised horizontally onto a regular longitude–latitude grid with Arakawa C-grid staggering (Arakawa and Lamb, 1977), whilst vertical decomposition is done via Charney–Phillips staggering (Charney and Phillips, 1953) using terrain-following hybrid height coordinates.

By convention, global configurations are defined on $2n$ longitudes and $1.5n + 1$ latitudes of scalar grid points with scalar and zonal wind variables at the north and south poles. This choice makes the grid spacing approximately isotropic in the mid-latitudes and means that the integer n, which represents the maximum number of zonal 2 grid-point waves that can be represented by the model, uniquely defines its horizontal resolution; a model with $n = 96$ is said to be N96 resolution. Limited-area configurations use a rotated longitude–latitude grid, usually with the pole rotated so that the grid's equator runs through the centre of the model domain.

In the vertical, the majority of climate configurations use an 85-level set labelled $\mathrm{L85}(50_\mathrm{t}, 35_\mathrm{s})_{85}$, which has 50 levels below 18 km (and hence at least sometimes in the troposphere), 35 levels above this (and hence solely in or above the stratosphere) and a fixed model lid 85 km above the surface. Limited-area climate simulations use a reduced 63-level set, $\mathrm{L63}(50_\mathrm{t}, 13_\mathrm{s})_{40}$, which has the same 50 levels below 18 km, with only 13 above and a lower model top at 40 km. Finally, NWP configurations use a 70-level set, $\mathrm{L70}(50_\mathrm{t}, 20_\mathrm{s})_{80}$ which has an almost identical 50 levels below 18 km, a model lid at 80 km, but has a reduced stratospheric resolution compared to $\mathrm{L85}(50_\mathrm{t}, 35_\mathrm{s})_{85}$. Although we have used a range of vertical resolutions in the stratosphere, a consistent tropospheric vertical resolution is used throughout. A more detailed description of these level sets is included in the Supplement to this paper.

The use of a consistent vertical resolution in the troposphere means that the atmospheric time step used is a function of horizontal resolution only. Simulations at N96 (approximately 135 km in the mid-latitudes) use a 20 min time step, whilst simulations at N512 (approximately 25 km in the mid-latitudes) use a 10 min time step. Limited-area simulations with resolutions of approximately 12 km typically use time steps of 5 min or less. A more complete list of time steps, along with other model parameters that change with horizontal or vertical resolution, is included in the Supplement.

2.2 Structure of the atmospheric model time step

A numerical model of the atmosphere requires adiabatic forcing and diabatic processes occurring on scales too fine to be resolved by the dynamical core to be treated by physical parametrisation schemes. The order of these schemes within the model time step and their coupling to the model's dynamics can be considered part of the design of the dynamical core. This requires a considered balance between stability, computational cost and both physical and numerical accuracy. The MetUM's time stepping treats slow timescale processes in parallel prior to the main advection step. This is followed by the fast timescale processes, which are treated sequentially, prior to the final dynamical solution (Staniforth et al., 2002). In this framework, the slow processes include radiation, large-scale precipitation and gravity wave drag, whilst the fast processes include atmospheric (boundary layer) turbulence, convection and coupling to the land surface model. Prognostic cloud variables and tracers such as aerosols are advected by the semi-Lagrangian dynamics. Their sources and sinks occur where appropriate within the physical parametrisation schemes (e.g. phase changes in the microphysics, wash-out in large-scale precipitation and mixing in the boundary layer and turbulence schemes). Chemical and physical process internal to the aerosol scheme occur at the end of the time step. The descriptions of these parametrisation schemes below are arranged in an order appropriate to their place within the model time step.

2.3 Solar and terrestrial radiation

Shortwave (SW) radiation from the Sun is absorbed in the atmosphere and at the Earth's surface and provides energy to drive the atmospheric circulation. Longwave (LW) radiation is emitted from the planet into space and redistributes heat

[1] Where the configurations remain unchanged from GA3.0 and GL3.0, Sect. 2 contains material which is unaltered from the documentation paper for that release (Walters et al., 2011).

[2] In addition to the material herein, the Supplement to this paper includes a short list of model settings outside the GA/GL definition that are dependent on either model resolution or system application.

within the atmosphere. These processes are parametrised via the radiation scheme, which provides prognostic atmospheric temperature increments and surface fluxes and additional diagnostic fluxes.

The radiation scheme of Edwards and Slingo (1996) is used with a configuration based on Cusack et al. (1999) with a number of significant updates. The correlated-*k* method is used for gaseous absorption with 6 bands in the SW and 9 bands in the LW. The method of equivalent extinction (Edwards, 1996) is used for minor gases in each band. Gaseous absorption coefficients are generated using the HITRAN 2001 spectroscopic database (Rothman et al., 2003) with updates up to 2003. The water vapour continuum is represented using version 2.4 of the Clough–Kneizys–Davies (CKD) model (Clough et al., 1989; Mlawer et al., 1999). Twenty-one (21) *k* terms are used for the major gases in the SW bands. Absorption by water vapour (H_2O), ozone (O_3), carbon dioxide (CO_2) and oxygen (O_2) is included. The treatment of O_3 absorption is as described in Zhong et al. (2008). The solar spectrum uses data from Lean (2000) at wavelengths shorter than 735 nm with the Kurucz and Bell (1995) spectrum at longer wavelengths. Forty-seven (47) *k* terms are used for the major gases in the LW bands. Absorption by H_2O, O_3, CO_2, CH_4, nitrous oxide (N_2O), CFC-11 (CCl_3F), CFC-12 (CCl_2F_2) and HFC134a (CH_2FCF_3) is included. For climate simulations, the atmospheric concentrations of CFC-12 and HFC134a are adjusted to represent absorption by all the remaining trace halocarbons. The treatment of CO_2 and O_3 absorption is as described in Zhong and Haigh (2000) to provide accurate stratospheric heating. Of the major gasses considered, only H_2O is prognostic; O_3 uses a zonally symmetric climatology, whilst other gasses are prescribed using either fixed or time-varying mass mixing ratios and assumed to be well mixed.

Absorption and scattering by the following categories of aerosol, either prognostic or climatological, are included in both the SW and LW: ammonium sulphate, mineral dust, sea salt, biomass burning, fossil-fuel black carbon, fossil-fuel organic carbon, and secondary organic (biogenic) aerosols. The parametrisation of cloud droplets is described in Edwards and Slingo (1996) using the method of "thick averaging". Padé fits are used for the variation with effective radius, which is computed from the number of cloud droplets. When using prognostic aerosol, this is derived from the aerosol concentrations (Jones et al., 1994, 2001); whilst when using either no aerosol or climatological aerosol, this is assumed to be 100 cm^{-3} for maritime air masses and 300 cm^{-3} for continental air masses. The parametrisation of ice crystals is described in Edwards et al. (2007). Full treatment of scattering is used in both the SW and LW. The sub-grid cloud structure is represented using the Monte Carlo Independent Column Approximation (McICA) as described in Hill et al. (2011), with optimal sampling using 6 extra terms in the LW and 10 in the SW for the reduction of random noise.

Full radiation calculations are made every 3 h using the instantaneous cloud fields (from the end of the previous time step) and a mean solar zenith angle for the following 3 h period. Corrections are made for the change in solar zenith angle on every model time step and the change in cloud fields every hour as described in Manners et al. (2009). The emissivity and the albedo of the surface are set by the land surface model. The direct SW flux at the surface is corrected for the angle and aspect of the topographic slope as described in Manners et al. (2012). The albedo of the sea surface uses a modified version of the parametrisation from Barker and Li (1995) with a varying spectral dependence.

2.4 Large-scale precipitation

The formation and evolution of precipitation due to grid scale processes is the responsibility of the large-scale precipitation – or microphysics – scheme, whilst small-scale precipitating events are handled by the convection scheme. The microphysics scheme has prognostic input fields of heat, moisture and cloud from the end of the previous time step, which it modifies in turn. The microphysics used is based on Wilson and Ballard (1999), with extensive modifications. We use a prognostic rain formulation, which allows three-dimensional advection of the precipitation particles. The particle size distribution for rain uses rain-rate dependent distribution of Abel and Boutle (2012). The minimum cloud liquid content for autoconversion to occur has been altered from the original Tripoli and Cotton (1980) formulation to a liquid content where the number of drops over 20 µm is 1000 m^{-3}, as discussed in Abel et al. (2010). In addition, we have used the fall velocities of Abel and Shipway (2007), which allow a better representation of the drizzle drop spectrum. We also make use of multiple sub-time-steps of the precipitation scheme, as in Posselt and Lohmann (2008) with one sub-time-step for every two minutes of the model time step to achieve a realistic treatment of in-column evaporation. When prognostic aerosols are used, the aerosol mass mixing ratios provide the cloud droplet number for autoconversion, according to the formulae of Jones et al. (1994, 2001). The aerosols which provide the droplet number are ammonium sulphate, sea salt, biomass burning and fossil-fuel organic carbon. When using either no aerosol or climatological aerosol, the cloud droplet number assumes the same land–sea split as in the radiation scheme.

2.5 Large-scale cloud

Clouds appear on sub-grid scales well before the humidity averaged over the size of a model grid box reaches saturation. A cloud parametrisation scheme is therefore required to determine the fraction of the grid box which is covered by cloud and the amount and phase of condensed water contained in those clouds. The formation of clouds will convert water vapour into liquid or ice and release latent heat. The

cloud cover and liquid and ice water contents are then used by the radiation scheme to calculate the radiative impact of the clouds and by the large-scale precipitation scheme to calculate whether any precipitation has formed.

The parametrisation used is the MetUM's prognostic cloud fraction and prognostic condensate (PC2) scheme (Wilson et al., 2008a, b) along with the modifications to the cloud erosion parametrisation described by Morcrette (2012). PC2 uses three prognostic variables for humidity mixing ratio – water vapour, liquid and ice – and a further three prognostic variables for cloud fraction: liquid, ice and total. The total cloud fraction is not necessarily equal to the sum of the other two due to the presence of mixed-phase regions. The following atmospheric processes can modify the cloud fields: shortwave radiation, longwave radiation, boundary layer processes, convection, precipitation, small-scale mixing (cloud erosion), advection and pressure changes due to large-scale vertical motion. The convection scheme calculates increments to the prognostic liquid and ice water contents by detraining condensate from the convective plume, whilst the cloud fractions are updated using the non-uniform forcing method of Bushell et al. (2003). One advantage of the prognostic approach is that clouds can be transported away from where they were created. For example, anvils detrained from convection can persist and be advected downstream long after the convection itself has ceased.

2.6 Orographic gravity wave drag

The effect of local and mesoscale orographic features not resolved by the mean orography, from individual hills through to small mountain ranges, must be parametrised. The smallest scales, where buoyancy effects are not important, are represented by an effective roughness parametrisation in which the roughness length for momentum used by the boundary layer scheme is increased over orography (Gregory et al., 1998). The effects of the remainder of the sub-grid orography (on scales where buoyancy effects are important) are parametrised by a flow-blocking and gravity wave drag parametrisation. The scheme is based on Webster et al. (2003) and accounts for drag effects due to sub-grid orography in stable conditions. The sub-grid orography is described in terms of its amplitude, which is proportional to the standard deviation of the source orography in a model grid box, and its anisotropy, i.e. how ridge-like the sub-grid orography is. The total surface stress is proportional to the bulk low-level winds and stability, and is determined using a simple linear hydrostatic expression; idealised modelling (e.g. Wells et al., 2005) suggests this captures the total surface stress reasonably well. The low-level Froude number is then used to partition the total stress into gravity wave and flow-blocking components due to flow over and around the orography respectively. The flow-blocking drag is diagnosed assuming a linear decrease in the stress over the depth of the sub-grid orography, whilst the gravity wave stress is launched upwards and a drag exerted at levels where wave breaking or wave saturation is diagnosed. Typically, in excess of 90 % of the global mean of the total surface stress is attributed to low-level flow blocking. The drag is applied as explicit increments to the model wind fields, so a numerical limiter is imposed on the flow-blocking drag to ensure the numerical stability of the scheme (Brown and Webster, 2004).

2.7 Non-orographic gravity wave drag

Non-orographic sources – such as convection, fronts and jets – can force gravity waves with non-zero phase speed. These waves break in the upper stratosphere and mesosphere, depositing momentum, which contributes to driving the zonal mean wind and temperature structures away from radiative equilibrium. Waves on scales too small for the model to sustain explicitly are represented by a spectral sub-grid parametrisation scheme (Scaife et al., 2002), which by contributing to this mechanism leads to a more realistic tropical quasi-biennial oscillation. The scheme, described in more detail in Walters et al. (2011), represents processes of wave generation, conservative propagation and dissipation by critical-level filtering and wave saturation acting on a vertical wavenumber spectrum of gravity wave fluxes following Warner and McIntyre (2001). Launched in the lower troposphere, the two-part spectrum is linear from low wavenumber cut-off up to a spectrum peak, corresponding to wavelengths of 20 km and 4.3 km, whilst beyond the peak an inverse cubic tail is characteristic of saturation. Current values chosen to scale the spectrum represent order 10 % of saturation spectrum amplitudes at launch height. Momentum conservation is enforced at launch, where isotropic fluxes guarantee zero net momentum, and by imposing a condition of zero vertical wave flux at the model upper boundary. In between, momentum deposition occurs in each layer where reduced integrated flux results from erosion of the launch spectrum, after transformation by conservative propagation, to match the locally evaluated saturation spectrum.

2.8 Atmospheric boundary layer

Turbulent motions in the atmosphere are not resolved by global atmospheric models, but are important to parametrise in order to give realistic vertical structure in the thermodynamic and wind profiles. Although referred to as the "boundary layer" scheme, this parametrisation represents mixing over the full depth of the troposphere. The scheme is that of Lock et al. (2000) with the modifications described in Lock (2001) and Brown et al. (2008). It is a first-order turbulence closure mixing adiabatically conserved heat and moisture variables, momentum and tracers. For unstable boundary layers, diffusion coefficients (K profiles) are specified functions of height within the boundary layer, related to the strength of the turbulence forcing. Two separate K profiles are used, one for surface sources of turbulence (surface heating and wind

shear) and one for cloud-top sources (radiative and evaporative cooling). The existence and depth of unstable layers is diagnosed initially by moist adiabatic parcels and then adjusted to ensure that the buoyancy consumption of turbulence kinetic energy is limited. This can permit the cloud layer to decouple from the surface (Nicholls, 1984). If cumulus convection is diagnosed (through comparison of cloud and sub-cloud layer moisture gradients), the surface-driven K profile is restricted to below cloud base and the mass flux convection scheme is triggered from that level. Mixing across the top of the boundary layer is through an explicit entrainment parametrisation that is coupled to the radiative fluxes and the dynamics through a sub-grid inversion diagnosis. If the thermodynamic conditions are right, cumulus penetration into a stratocumulus layer can generate additional turbulence and cloud-top entrainment in the stratocumulus by enhancing evaporative cooling at cloud top. There are additional non-local fluxes of heat and momentum in order to generate more vertically uniform potential temperature and wind profiles in convective boundary layers. For stable boundary layers and in the free troposphere, we use a local Richardson number scheme based on Smith (1990). Its stable stability dependence is given by the "sharp" function over sea and by the "MES-tail" function over land (which matches linearly between an enhanced mixing function at the surface and sharp at 200 m and above). This additional near-surface mixing is motivated by the effects of surface heterogeneity, such as those described in McCabe and Brown (2007). The resulting diffusion equation is solved implicitly using the monotonically damping, second-order-accurate, unconditionally stable numerical scheme of Wood et al. (2007). The kinetic energy dissipated through the turbulent shear stresses is returned to the atmosphere as a local heating term.

2.9 Convection

The convection scheme represents the sub-grid scale transport of heat, moisture and momentum associated with cumulus clouds within a grid box. The MetUM uses a mass flux convection scheme based on Gregory and Rowntree (1990) with various extensions to include down-draughts (Gregory and Allen, 1991) and convective momentum transport (CMT). The current scheme consists of three stages: (i) convective diagnosis to determine whether convection is possible from the boundary layer; (ii) a call to the shallow or deep convection scheme for all points diagnosed deep or shallow by the first step; and (iii) a call to the mid-level convection scheme for all grid points.

The diagnosis of shallow and deep convection is based on an undilute parcel ascent from the near surface for grid boxes where the surface layer is unstable and forms part of the boundary layer diagnosis (Lock et al., 2000). Shallow convection is then diagnosed if the following conditions are met: (i) the parcel attains neutral buoyancy below 2.5 km or below the freezing level, whichever is higher, and (ii) the air in model levels forming a layer of order 1500 m above this has a mean vertical velocity less than $0.02\,\mathrm{m\,s^{-1}}$. Otherwise, convection diagnosed from the boundary layer is defined as deep.

The deep convection scheme differs from the original Gregory and Rowntree (1990) scheme in using a convective available potential energy (CAPE) closure based on Fritsch and Chappell (1980). Mixing detrainment rates now depend on relative humidity and forced detrainment rates adapt to the buoyancy of the convective plume (Derbyshire et al., 2011). The CMT scheme uses a flux gradient approach (Stratton et al., 2009).

The shallow convection scheme uses a closure based on Grant (2001) and has larger entrainment rates than the deep scheme consistent with cloud-resolving model (CRM) simulations of shallow convection. The shallow CMT uses flux–gradient relationships derived from CRM simulations of shallow convection (Grant and Brown, 1999).

The mid-level scheme operates on any instabilities found in a column above the top of deep or shallow convection or above the lifting condensation level. The scheme is largely unchanged from Gregory and Rowntree (1990), but uses the Gregory et al. (1997) CMT scheme and a CAPE closure. The mid-level scheme operates mainly either overnight over land when convection from the stable boundary layer is no longer possible or in the region of mid-latitude storms. Other cases of mid-level convection tend to remove instabilities over a few levels and do not produce much precipitation.

The timescale for the CAPE closure, which is used for the deep and mid-level convection schemes, is essentially fixed at a chosen value of one hour; however, if extremely high large-scale vertical velocities are detected in the column then the timescale is rapidly reduced to ensure numerical stability.

2.10 Atmospheric aerosols and chemistry

As discussed in Walters et al. (2011), the modelling of atmospheric aerosols and chemistry is considered as a separate component of the full Earth system and remains outside the scope of this document. The aerosol species represented and their interaction with the atmospheric parametrisations is, however, part of the Global Atmosphere component and has therefore been included in the descriptions above. Systems including prognostic aerosol modelling do so using the CLASSIC (Coupled Large-scale Aerosol Simulator for Studies in Climate) aerosol scheme described in Bellouin et al. (2011). The treatment of tropospheric aerosols in systems which do not model these explicitly is supplemented by the use of a three-dimensional monthly climatology for each aerosol species, although currently these are only used to model the direct aerosol effect. In addition to the treatment of these tropospheric aerosols, we include a simple stratospheric aerosol climatology based on Cusack et al. (1998). We also include the production of stratospheric water vapour

via a simple methane oxidation parametrisation (Untch and Simmons, 1999).

2.11 Land surface and hydrology: Global Land 4.0

The exchange of fluxes between the land surface and the atmosphere is an important mechanism for heating and moistening the atmospheric boundary layer. In addition, the exchange of CO_2 and other greenhouse gases plays a significant role in the climate system. The hydrological state of the land surface contributes to impacts such as flooding and drought as well as providing freshwater fluxes to the ocean, which influences ocean circulation. Therefore, a land surface model needs to be able to represent this wide range of processes over all surface types that are present on the Earth.

The Global Land configuration uses a community land surface model, JULES (Best et al., 2011; Clark et al., 2011), to model all of the processes at the land surface and in the sub-surface soil. JULES is based on a combination of the Met Office Surface Exchange Scheme (MOSES, Cox et al., 1999) and the TRIFFID (Top-down Representation of Interactive Foliage and Flora Including Dynamics) dynamic vegetation model (Cox et al., 2000; Cox, 2001). A tile approach is used to represent sub-grid scale heterogeneity (Essery et al., 2003), with the surface of each land point subdivided into five types of vegetation (broadleaf trees, needle-leaved trees, temperate C3 grass, tropical C4 grass and shrubs) and four non-vegetated surface types (urban areas, inland water, bare soil and land ice). Vegetation canopies are represented in the surface energy balance through the coupling to the underlying soil. This canopy is coupled via radiative and turbulent exchange, whilst any bare soil component couples through conduction. JULES also uses a canopy radiation scheme to represent the penetration of light within the vegetation canopy and its subsequent impact on photosynthesis (Mercado et al., 2007). The canopy also interacts with the surface snow. For most vegetation types, the snow is held on top of the canopy, whilst for needle-leaved trees some of the snow is intercepted by the canopy and the remainder is held beneath it. This impacts the surface albedo, the snow sublimation and the snow melt. The vegetation canopy code has been adapted for use with the urban surface type by defining an "urban canopy" with the thermal properties of concrete (Best, 2005). This has been demonstrated to give improvements over representing an urban area as a rough bare soil surface. Similarly, this canopy approach has also been adopted for the representation of lakes. The original representation in MOSES was through a soil surface that could evaporate at the potential rate (i.e. a soggy soil), which has been shown to have incorrect seasonal and diurnal cycles for the surface temperature (Rooney and Jones, 2010). By defining an "inland water canopy" and setting the thermal characteristics to those of a suitable depth of water (taken to be 1 m), a better diurnal cycle for the surface temperature is achieved.

Surface fluxes are calculated separately on each tile using surface similarity theory. In stable conditions we use the similarity functions of Beljaars and Holtslag (1991), whilst in unstable conditions we take the functions from Dyer and Hicks (1970). The effects on surface exchange of both boundary layer gustiness (Godfrey and Beljaars, 1991) and deep convective gustiness (Redelsperger et al., 2000) are included. Temperatures at 1.5 m and winds at 10 m are interpolated between the model's grid levels using the same similarity functions, but a parametrisation of transitional decoupling in very light winds is included in the calculation of the 1.5 m temperature.

Soil processes are represented using a 4-layer scheme for the heat and water fluxes with hydraulic relationships taken from van Genuchten (1980). These four soil layers have thicknesses from the top down of 0.1, 0.25, 0.65 and 2.0 m. The impact of moisture on the thermal characteristics of the soil is represented using a simplification of Johansen (1975), as described in Dharssi et al. (2009). The energetics of water movement within the soil is accounted for, as is the latent heat exchange resulting from the phase change of soil water from liquid to solid states. Sub-grid scale heterogeneity of soil moisture is represented using the Large-Scale Hydrology approach (Gedney and Cox, 2003), which is based on the topography-based rainfall-runoff model TOPMODEL (Beven and Kirkby, 1979). This enables the representation of an interactive water table within the soil that can be used to represent wetland areas, as well as increasing surface runoff through heterogeneity in soil moisture driven by topography.

A river routing scheme is used to route the total runoff from inland grid points both out to the sea and to inland basins, where it can flow back into the soil moisture. Excess water in inland basins is distributed evenly across all sea outflow points. In coupled model simulations the resulting freshwater outflow is passed to the ocean, where it is an important component of the thermohaline circulation, whilst in atmosphere/land-only simulations this ocean outflow is purely diagnostic. River routing calculations are performed using the TRIP (Total Runoff Integrating Pathways) model (Oki and Sud, 1998), which uses a simple advection method (Oki, 1997) to route total runoff along prescribed river channels on a $1^\circ \times 1^\circ$ grid using a 3 h time step. Land surface runoff accumulated over this time step is mapped onto the river routing grid prior to the TRIP calculations, after which soil moisture increments and total outflow at river mouths are mapped back to the atmospheric grid (Falloon and Betts, 2006). A validation of the river routing scheme in much older coupled model configurations is presented in Falloon et al. (2011). This river routing model is not currently being used in limited-area or NWP implementations of the Global Atmosphere/Land.

Table 1. Source data sets used to create standard ancillary files used in GA4.0/GL4.0.

Ancillary field	Source data	Notes
Land mask/fraction	System dependent	
Mean/sub-grid orography	GLOBE 30″; Hastings et al. (1999)	Fields filtered before use
Land usage	IGBP; Global Soil Data Task (2000)	Mapped to 9 tile types
Soil properties	HWSD; Nachtergaele et al. (2008)	
Leaf area index/canopy height	MODIS collection 5	4 km data (Samanta et al., 2012) mapped to 5 plant types
TOPMODEL topographic index	(Verdin and Jensen, 1996)	
SST/sea ice	System/experiment dependent	
Ozone	SPARC-II; Cionni et al. (2011)	Zonal mean field used
Aerosol emissions/fields:		Only required for prognostic aerosols
Main primary emissions	CMIP5; Lamarque et al. (2010)	Includes SO_2, DMS, soot, OCFF, biomass burning
Volcanic SO_2 emissions	Andres and Kasgnoc (1998)	
Sulphur-cycle offline oxidants	STOCHEM* (Derwent et al., 2003)	
Ocean DMS concentrations	Kettle et al. (1999)	
Biogenic aerosol ancillary	STOCHEM*; Derwent et al. (2003)	
CLASSIC aerosol ancillaries	System/experiment dependent	Used when prognostic fields not available
TRIP river paths	1 ° data from Oki and Sud (1998)	Adjusted at coastlines to ensure correct outflow

* Note that STOCHEM denotes that these fields are derived from runs of the STOCHEM chemistry model.

2.12 Ancillary files and forcing data

In the MetUM, the characteristics of the lower boundary, the values of climatological fields and the distribution of natural and anthropogenic emissions are specified using ancillary files. Use of correct ancillary file inputs can play as important a role in the performance of a system as the correct choice of options in the parametrisations described above, but this is often overlooked by both users and developers. For this reason, we consider the source data and processing required to create ancillaries as part of the definition of the Global Atmosphere/Land configurations.

Table 1 contains the main ancillaries used in GA4.0/GL4.0 as well as references to the source data from which they are created.

3 Developments since Global Atmosphere/Land 3.0

In this section, we describe the main developments in the Global Atmosphere and Global Land configurations since GA3.0/GL3.0.

3.1 Dynamical formulation and discretisation

The formulation of the dynamical core in GA4.0 is largely identical to that in GA3.0. One change that has been made, however, is the replacement of the specific quantities for moist prognostics (such as specific humidity) with mass mixing ratios as described in Davies et al. (2005). This change has been made in preparation for the future inclusion of the "ENDGame" dynamical core (Wood et al., 2013), which is formulated solely in terms of mass mixing ratios. These mass mixing ratios are also used by the parallel physical parametrisations described in Sect. 2.2, but are still converted into specific quantities for use in the sequential physics. The necessary conversions take place within each model time step.

3.2 Solar and terrestrial radiation

The only change made to the radiation scheme in GA4.0 is a correction to the treatment of shortwave fluxes in the coupling to the sea ice component of coupled modelling systems at grid points with fractional land cover. This correction ensures that the shortwave flux to sea ice points is accounted for on every atmospheric model time step, rather than only on the time steps in which the fluxes were calculated, which was the case in GA3.0.

3.3 Large-scale precipitation

The main change to the large-scale precipitation scheme since GA3.0 has been the introduction of an improved particle size distribution for rain (Abel and Boutle, 2012). In both the GA3.0 and GA4.0 configurations, the single-moment rain particle size distribution is defined as a function of diameter:

$$N(D) = N_0 D^{\alpha} \exp(-\lambda D), \quad (1)$$

Table 2. Changes to the rain particle size distribution parameters between GA3.0 and GA4.0.

Configuration	x_1	x_2
GA3.0; Walters et al. (2011); Abel et al. (2010)	26.20	1.57
GA4.0; Abel and Boutle (2012)	0.22	2.20

where $N(D)$ is the number of particles of diameter D. The shape parameter, α, is set to zero in both GA3.0 and GA4.0, which is shown by Abel and Boutle (2012) to be a reasonable assumption. Equation (1), therefore, reduces to a function of the slope parameter λ and the intercept parameter N_0. The intercept parameter is defined as

$$N_0 = x_1 \lambda^{x_2}, \tag{2}$$

where x_1 and x_2 are dimensionless constants. The slope parameter is defined as a function of rain mixing ratio q_r and air density ρ using

$$\lambda = \frac{\pi \rho_\mathrm{w} x_1 \Gamma(4)}{6 \rho q_\mathrm{r}}^{\frac{1}{4-x_2}}, \tag{3}$$

where ρ_w is the density of water ($1000\,\mathrm{kg\,m^{-3}}$). The values of x_1 and x_2 for GA3.0 and GA4.0 are shown in Table 2. The values chosen for GA3.0 were intended to allow a larger number of smaller rain drops to be produced in light rain and drizzle conditions. However, Abel and Boutle (2012) showed that the GA3.0 values did not correctly capture the variability in N_0 observed in aircraft and lidar data, particularly near the drizzle end of the spectrum. They proposed the new values shown in Table 2, which have been implemented in GA4.0.

Figure 1 shows the impact of this change on the droplet size distribution for three rain mixing ratios. For the smallest mixing ratio, the intercept of the particle size distribution is at least ten times greater in GA4.0 than GA3.0, whilst for the highest mixing ratio the two lines are very similar.

Two other minor changes have been made since GA3.0. The first is a correction to the freezing of rain. The prognostic rain formulae introduced at GA3.0 allow small amounts of supercooled rain to remain in the atmosphere at altitudes above 10 km. We have applied a homogeneous freezing of this rain to ice at temperatures less than or equal to $-40\,^\circ$C. A heterogeneous freezing of rain is being developed, but has not been implemented for GA4.0. Secondly, we make a change to the sub-stepping. The microphysics scheme processes each grid box in the column, starting from the top of the atmosphere and finishing at the surface. In GA3.0 this was performed by a number of iterations on each model level, before proceeding to the next level down in the vertical. For GA4.0, this has changed so that the microphysics iterations are performed over the whole column; each iteration processes every model level once and the next iteration starts at the top of the atmosphere. The change to iterations looping over columns rather than over model levels was made as it was thought to be more physically realistic, effectively giving the scheme a shorter time step than the rest of the MetUM.

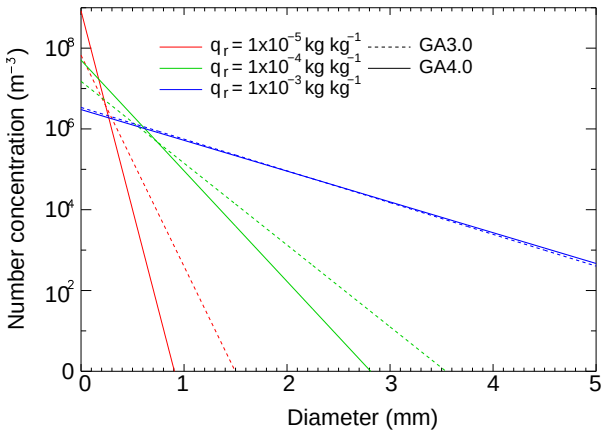

Fig. 1. The difference between the GA3.0 particle size distribution and the GA4.0 particle size distribution, taken from Abel and Boutle (2012) for three different values of the rain mixing ratio (q_r).

3.4 Large-scale cloud

By studying the prognostic cloud scheme's cloud tendency terms, Morcrette and Petch (2010) found a spurious feedback caused by an explicit link between the rate of sub-grid homogenisation in the cloud erosion parametrisation and the relative humidity. For this reason, an alternative way of calculating the cloud erosion term has been developed for use in GA4.0 (Morcrette, 2012). The new formulation relates the rate of mixing to the cloud fraction, so that the maximum mixing will occur when the sky is half covered in cloud. The mixing tends to zero as the cloud fraction approaches zero or one, where there are no cloud edges across which the mixing of clear and cloudy air can occur. In summary, the new cloud erosion parametrisation consists of calculating the change in the prognostic grid-box-mean liquid water content, $\overline{q_\mathrm{cl}}$, using

$$\left.\frac{\partial \overline{q_\mathrm{cl}}}{\partial t}\right|_\mathrm{Erosion} = \alpha K C_\mathrm{l}(1 - C_\mathrm{l})(q_\mathrm{sat} - q_\mathrm{v}), \tag{4}$$

where C_l is the liquid cloud fraction, q_sat and q_v are the saturation mixing ratio and water vapour mixing ratio respectively, α is a geometric factor taking a value of $1/3$ and K is the erosion coefficient, which has a value of $3.0 \times 10^{-4}\,\mathrm{s^{-1}}$ in GA4.0. The rate of sub-grid homogenisation of the moisture probability density function, consistent with this change in liquid water content, is found from Eq. (A11) in Wilson et al. (2008a). This is then used to calculate the change in liquid cloud fraction using their Eq. (A12) as before.

The large-scale precipitation scheme calculates the rate with which frozen condensate falls from one layer to the next. In addition, the PC2 cloud scheme represents how the falling

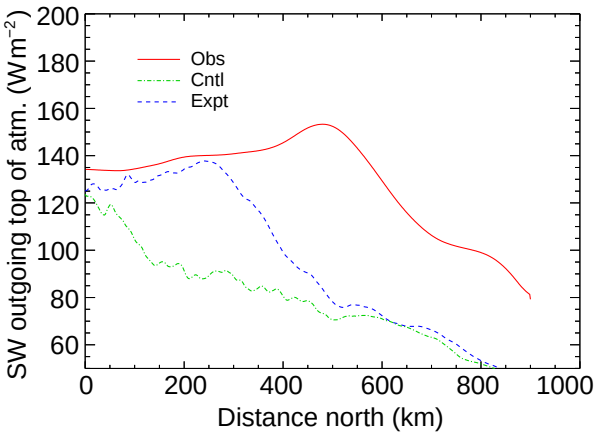

Fig. 2. Top-of-atmosphere reflected shortwave along a meridional flight track from a cold-air outbreak case within the CONSTRAIN field campaign. The solid line (Obs) is aircraft observations made at about 11:00 UTC on 31 January 2010; the dotted line (Cntrl) is a 17 h forecast from the 1.5 km-resolution limited-area MetUM NWP configuration (UKV) valid at the same time as the observations, and the dashed line (Expt) is from an equivalent UKV forecast including the shear-dominated boundary layer diagnosis.

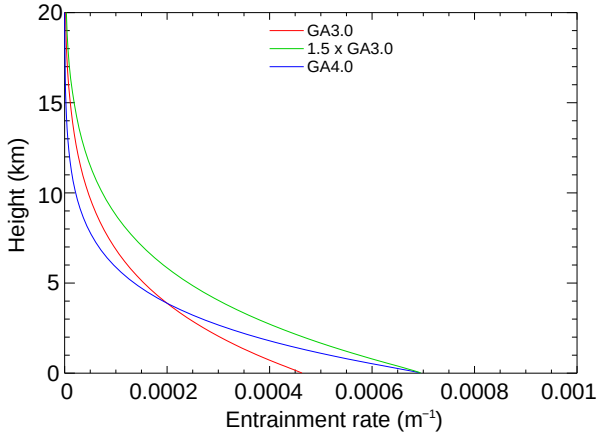

Fig. 3. Entrainment rate profiles for deep convection (in height co-ordinates) used in GA3.0, GA4.0 and that used in Klingaman and Woolnough (2013) labelled 1.5× GA3.0.

ice will increase the ice cloud fraction in the layer it enters. In the absence of shear, the ice cloud fraction is advected downwards using the ice fall velocity. Any ice cloud fraction falling into clear air is then rescaled in the horizontal by assuming it has filled the grid box in the vertical.

In the presence of shear, the falling ice cloud fraction can be displaced laterally as it falls, making it less likely to fall into the vertically contiguous cloud below and more likely to fall into clear air. In Wilson et al. (2008a) and GA3.0, this source term was calculated assuming that the vertical wind shear had a globally constant value of $1.5 \times 10^{-4}\,s^{-1}$ and did not alter with the size of the model grid box. In GA4.0, the wind-shear term is calculated from the vertical shear of the model's horizontal wind, and the potential increase in ice cloud fraction due to the lateral displacement of the ice cloud as it falls is related to the size of the grid box (which varies between systems using different horizontal resolutions as well as with latitude in any one system due to the model's latitude–longitude grid).

This falling ice parametrisation assumes that, although ice may fall out of a layer and increase the ice cloud fraction in the layers below, the ice cloud fraction remains constant in the layer the ice is falling from. These layers lose mass as ice falls out, but their lateral extent remains constant. This represents the ice cloud becoming optically thinner whilst maintaining its lateral extent.

Wilson et al. (2008b) describe how the temperature at which condensate in the convection scheme changes from liquid to ice had been set to −10 °C when using PC2, which allows the convection scheme to be a source of super-cooled liquid water. In Wilson et al. (2008b) and GA3.0, the phase of the detrained condensate would change abruptly from liquid to ice as the temperature dropped below this threshold. In GA4.0 this abrupt change has been replaced by a gradual transition, linearly applied between temperatures of 0 °C and −20 °C, which is physically more realistic.

3.5 Atmospheric boundary layer

A significant long-standing radiative bias in the model is a north–south asymmetry in reflected SW, in which the planet is too bright in the Northern Hemisphere and too dark over the Southern Ocean. Bodas-Salcedo et al. (2012) undertook a detailed diagnostic analysis to understand the origin of cloud biases over the Southern Ocean. This showed that the model produced too-little cloud in cold-air outbreaks. Data from a cold-air outbreak case off northwest Scotland, investigated as part of the CONSTRAIN field campaign, were used to further understand the bias and develop a revision to the boundary layer regime diagnosis in situations of strong wind shear.

They hypothesised that shear-generated turbulence could extend mixing into regions of weak static stability, such as across the base of a cumulus cloud layer. An additional dynamical constraint was therefore added that would suppress the (thermodynamically diagnosed) triggering of the convection scheme. Instead, the boundary layer scheme's non-local diffusion profiles would be used to parametrise the mixing right up to cloud top. This diagnosis is made by inspecting the profile of the local Richardson number (Ri). If $Ri < 0.25$ both below cloud base and throughout the lower fraction of the cloud layer, then a "shear-dominated boundary layer" is diagnosed. The wind shear is assumed to disrupt the formation of cumulus clouds and we model a more appropriate, well-mixed stratocumulus-topped boundary layer type. The fraction of the cloud layer through which to continue the Ri test is defined by the parameter f (Bodas-Salcedo et al., 2012). Figure 2 shows results from a test of this change in

Table 3. Changes to the ratio of the thermal to the momentum roughness lengths (z_{0h}/z_{0m}) for each surface type between GL3.0 and GL4.0.

Surface type	z_{0h}/z_{0m} (GL3.0)	z_{0h}/z_{0m} (GL4.0)
Broadleaf trees	0.10	1.65
Needle-leaved trees	0.10	1.65
C3 grass	0.10	0.10
C4 grass	0.10	0.10
Shrubs	0.10	0.10
Urban	0.10	1×10^{-7}
Lake	0.10	0.25
Bare soil	0.10	0.02
Land ice	0.10	0.20
Sea ice	1.00	0.20

Table 4. Changes to the surface emissivity (ϵ) for each surface type between GL3.0 and GL4.0.

Surface type	ϵ (GL3.0)	ϵ (GL4.0)
Broadleaf trees	0.97	0.980
Needle-leaved trees	0.97	0.990
C3 grass	0.97	0.980
C4 grass	0.97	0.980
Shrubs	0.97	0.980
Urban	0.97	0.970
Lake	0.97	0.985
Bare soil	0.97	0.900
Land ice	0.97	0.990
Open sea	1.00	0.985
Sea ice	1.00	0.976

a 1.5 km-resolution limited-area MetUM forecast compared to observations taken during the CONSTRAIN field campaign (Field et al., 2013). At this resolution, which is much higher than that used in any Global Atmosphere configurations, the convection is assumed to be resolved and so the convection parametrisation is switched off, but the boundary layer diagnosis remains almost identical to that in the global model. The control configuration shows a significant underestimate of the liquid water path and reflected shortwave flux, which coincides with a region of stratiform cloud that appears in the model as a broken cloud layer with too-little cloud cover. Including shear-dominated boundary layer diagnosis (with $f = 0.5$) greatly decreases the frequency of cumulus convection diagnosis in favour of well-mixed cloud-capped layers and results in a significant enhancement to the reflected SW flux. In Global Atmosphere configurations (with parametrised convection), a series of sensitivity tests suggested a value of $f = 0.3$ would be more effective at both typical NWP and climate resolutions, suggesting a sensitivity to whether the cumulus transports were resolved or parametrised (rather than resolution itself).

Changes have also been made to the stability functions for momentum (f_m) and sensible heat (f_h) used in the Richardson number-dependent part of the boundary layer scheme. On the unstable side, the "conventional" model of Brown (1996) has been implemented that has the following dependence on the local Richardson number, *Ri*:

$$f_m = (1 - b_{LEM} Ri)^{1/2}; \quad (5)$$

$$f_h = \frac{1}{Pr_N} (1 - b_{LEM} Ri)^{1/2}, \quad (6)$$

where the constant $b_{LEM} = 1.43$ and Pr_N is the neutral Prandtl number. The previous functions gave significantly larger mixing in an attempt to represent the effects of non-local mixing in unstable boundary layers but this is no longer necessary when the non-local scheme is used. At the same time, a more realistic value for Pr_N of 0.7 has been introduced (a value of unity was used before). Large-eddy simulations (LES) of stable boundary layers and surface field site observations also tend to show an increase in Prandtl number with stability (e.g. Anderson, 2009). This is generally believed to represent the effects of gravity waves in transporting momentum but not heat or other scalars (hence the ratio of momentum to heat mixing increases). High-resolution LES of idealised stable boundary layers based on Beare et al. (2006) have motivated the formulation implemented here of $Pr = 0.7(1 + 2Ri)$. For model stability (and to keep within observed limits) *Pr* is capped at a maximum value of 5. The combined impact of both these changes on the stability functions is small.

3.6 Convection

At GA4.0 the code version used for the convection scheme was changed to allow greater flexibility for future developments. As part of this change the convective energy correction of Gregory and Rowntree (1990) was removed as its formulation was considered incorrect, never having been revised to take account of convective increments to cloud liquid and cloud ice. It is hoped to include a new revised convective energy correction in the future, which will be consistent with the scheme.

GA4.0 includes a revision to the convective entrainment and detrainment rates used in deep convective ascents. The entrainment rate was increased at lower levels in an attempt to gain some of the benefit seen in recent sensitivity studies, in which the entrainment rate was increased throughout the depth of the profile (Klingaman and Woolnough, 2013; Bush et al., 2012). Increasing the entrainment rate by a factor of 1.5 was shown to improve the simulation of the Madden–Julian Oscillation, tropical cyclones and the distribution of dry days and wet days over tropical land, but tends to increase the upper tropical tropospheric cold bias and degrade upper-level tropical winds. Figure 3 shows the deep entrainment profile

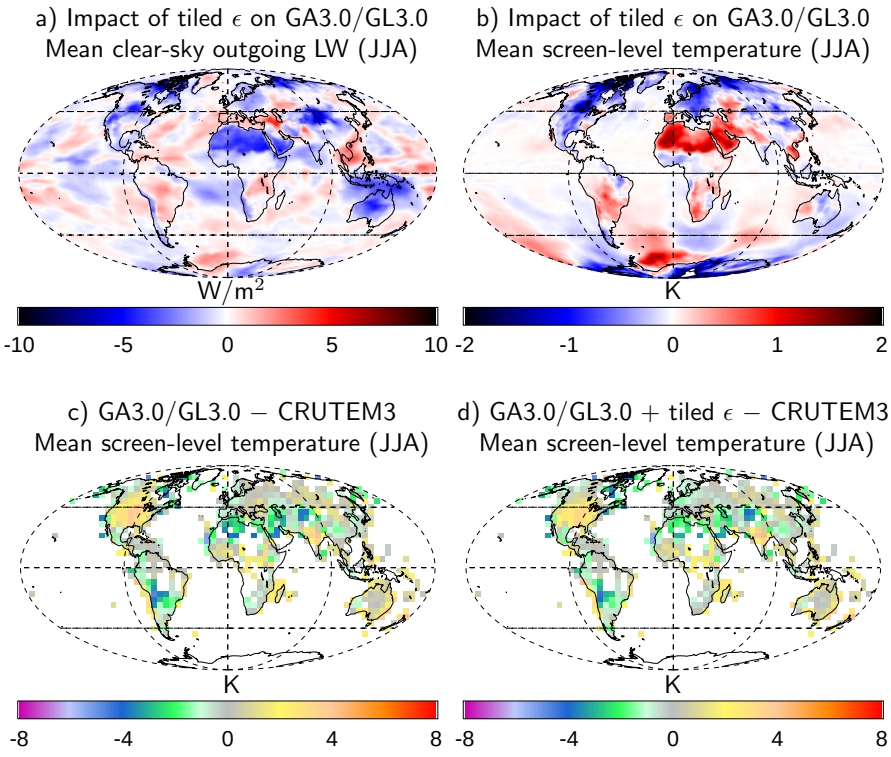

Fig. 4. Impact of the tiled emissivity ϵ on **(a)** the mean clear-sky outgoing LW radiation and **(b)** the mean screen-level temperature during JJA in a 10 yr N96 atmosphere/land-only climate simulation as well as the screen-level temperature errors in **(c)** the control simulation and **(d)** the test simulation against the CRUTEM3 climatology (Brohan et al., 2006).

used in GA4.0 (in height coordinates), which was chosen to match 1.5 times the GA3.0 entrainment rate at lower levels, but decreases with height (in coordinates of pressure P divided by the surface pressure P_*) by a factor of $(P/P_*)^2$ rather than P/P_* as was used in GA3.0. Whilst this did restrict the upper-level temperature and wind detriments seen in previous studies, it was also found to have little impact on the modes of variability that were improved in those studies. The mixing detrainment rate coefficient was increased by a factor of two to a value of 3.0, closer to the value of 6.0 suggested by a recent CRM study (Stirling and Stratton, 2012). Increasing mixing detrainment tends to increase the humidity in the lower tropical troposphere.

Finally, we have made changes to the treatment of the complex microphysical processes that occur in convective clouds, which are represented in a very simple manner within the convection scheme. The scheme defines a critical convective cloud condensate profile, $X_{\min}$, which is the minimum amount of condensate that a convective parcel at a given level must hold before precipitation will occur. Any condensate above this threshold will be precipitated out of the parcel; therefore $X_{\min}$ also defines the maximum amount of condensate that the parcel can hold after precipitation. This is an important quantity because it determines the precipitation efficiency of the convection scheme, and because it controls how much condensate, and hence also how much large-scale cloud fraction, is detrained from the convective parcel into the prognostic cloud variables. At GA4.0, $X_{\min}$ is defined as

$$X_{\min} = \begin{cases} q_{\mathrm{cl,max}} & \text{if } K q_{\mathrm{sat}}^{\mathrm{env}} > q_{\mathrm{cl,max}} \\ K q_{\mathrm{sat}}^{\mathrm{env}} & \text{if } q_{\mathrm{cl,max}} \geq K q_{\mathrm{sat}}^{\mathrm{env}} \geq q_{\mathrm{cl,min}} \\ q_{\mathrm{cl,min}} & \text{if } K q_{\mathrm{sat}}^{\mathrm{env}} < q_{\mathrm{cl,min}} \end{cases}, \quad (7)$$

where K is a factor (set to 0.5) that scales the local saturated specific humidity $q_{\mathrm{sat}}^{\mathrm{env}}$. $X_{\min}$ is limited to be between $q_{\mathrm{cl,min}}$, which has a value of $0.3\,\mathrm{g\,kg^{-1}}$, and $q_{\mathrm{cl,max}}$, which has a value of $1.5\,\mathrm{g\,kg^{-1}}$.

Prior to GA4.0, a similar functional form was used for $X_{\min}$, but two additional scalings were applied: it was increased at low levels to prevent shallow convection from precipitating and it was increased below the freezing level over land to reflect the higher concentration of cloud condensation nuclei. These additional scalings have been removed at GA4.0 because this additional level of complexity was difficult to justify, considering the extremely simple nature of this overall approach; this has been partially offset by increasing $q_{\mathrm{cl,max}}$ to the value quoted above.

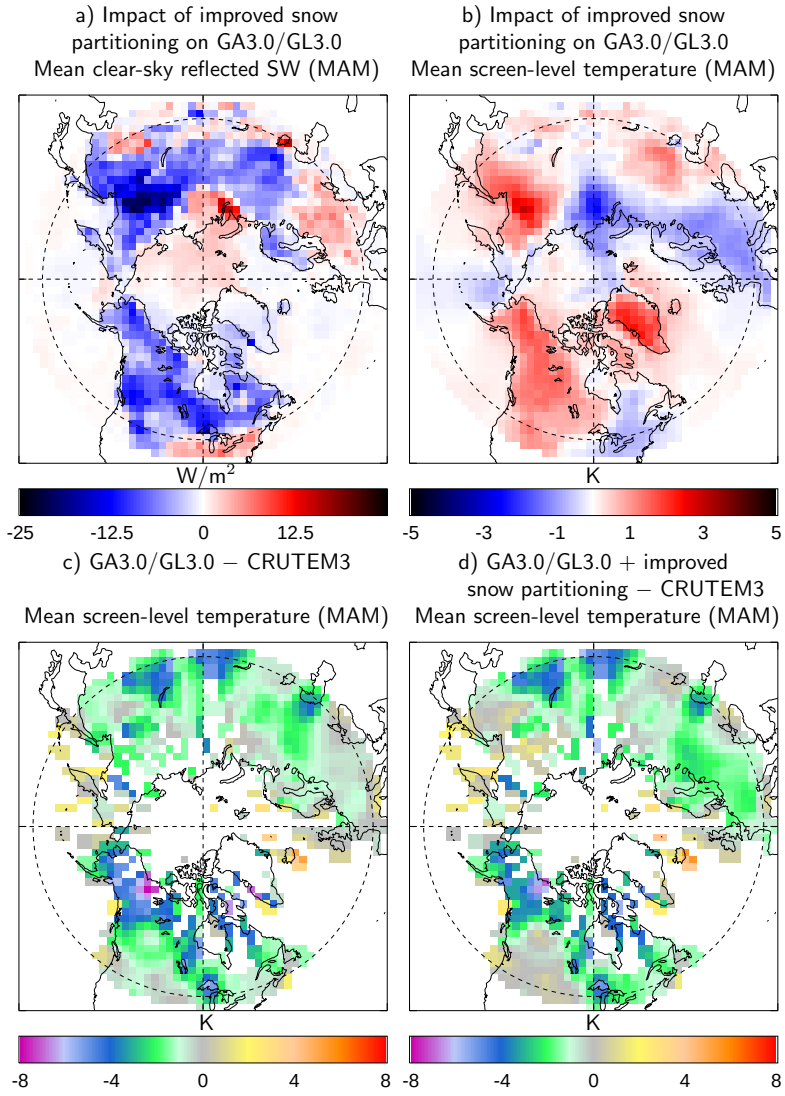

Fig. 5. Impact of the improved partitioning of snow on the mean clear-sky reflected SW radiation and screen-level temperature during MAM in a 10 yr N96 atmosphere/land-only climate simulation using the same format as Fig. 4.

3.7 Atmospheric aerosols and chemistry

The aerosol scheme was changed at GA4.0 to include the effect of seasonal vegetation dieback on dust emissions. This is achieved by calculating the dust emissions using the same method as before (see Woodward, 2011, for details), but scaling the emissions by a "dust emitting radiative bare soil fraction" of each grid box rather than the "permanent bare soil fraction". The radiative bare soil fraction, which is used to calculate the land surface model's albedo, is derived for each grid box from the MODIS collection 5 leaf area index (LAI) product, whilst we define the dust-emitting part of this as the total contribution from areas of permanent bare soil and seasonal grasses, as well as 50 % of the contribution from seasonal shrubs.

3.8 Land surface and hydrology: Global Land 4.0

The main aims during the development of GL4.0 were to improve the model's near-surface air temperature and to consolidate the differences between the previous GL3.0 "trunk" configuration and the GL3.1 "branch" used in operational global NWP forecasting (Walters et al., 2011). In GL3.0, the momentum roughness length of bare soil was set to 3×10^{-4} m, whilst in GL3.1 it was 3.2×10^{-3} m. Observational estimates of the roughness length of bare soil surfaces suggest large geographical variations covering this range (Greeley et al., 1997; Laurent et al., 2005), so we have adopted an intermediate value of 1×10^{-3} m for GL4.0. A momentum roughness length of 3×10^{-4} m over lakes was used in both GL3.0 and GL3.1. Comparisons between the

model and reanalyses suggest that GL3.0 suffers from a slow bias in the near-surface wind speed around the Great Lakes, so this value was reduced to 1×10^{-4} m, which is more consistent with the values predicted from wind-speed-dependent parametrisations over open water.

In order to improve the representation of near-surface temperature gradients and surface fluxes, the ratios of the thermal to the momentum roughness lengths (z_{0h}/z_{0m}) have also been revised, to the values shown in Table 3. GL3.0 assumed identical values of z_{0h} and z_{0m} over sea ice, which has been shown to lead to excessive latent heat fluxes (Birch et al., 2009) and is out of line with theoretical models and field measurements (Andreas, 1987; Andreas et al., 2010). In the longer term, we intend to investigate parametrisation of the ratio in terms of the roughness Reynolds number, but for the present the ratio has been reduced to a more typical value of 0.2 for both marginal and pack ice. Over land surfaces, the ratio z_{0h}/z_{0m} was set to 0.1 for all surface types in GL3.0. For land ice the ratio has been adjusted to 0.2, to be consistent with sea ice. Comparison of the modelled surface skin temperature with retrieved values over arid regions in GL3.1, in conjunction with observations of near-surface air temperature, suggested a significant underestimate of the near-surface temperature gradient. To improve this and in combination with the revision of z_{0m}, z_{0h}/z_{0m} for bare soil has been decreased to 0.02. Over lakes, the ratio has been set to 0.25, to be consistent with the revised momentum roughness length for lakes and the parametrisation of the ratio used over open sea. For vegetated surfaces, it has been argued that the ratio z_{0h}/z_{0m} should increase with canopy height (e.g. Chen and Zhang, 2009). In GL4.0, $z_{0h}/z_{0m} = 0.1$ for low vegetation, as in GL3.0, but for trees the ratio has been increased to 1.65, following Mölder and Lindroth (1999), who argue that the transfer of heat is more efficient than that of momentum in the deep roughness sublayer above tall vegetation. Over urban surfaces, z_{0h}/z_{0m} has been reduced to 10^{-7} for consistency with high-resolution forecasting models.

In GL3.0, the surface emissivity was set to 0.97 over all land surface tiles and to 1.0 over both open sea and sea ice. In GL4.0, each surface type is assigned a different emissivity, as shown in Table 4. These values are based on the data of Snyder et al. (1998), but in the case of bare soil we have also taken account of the emissivities used in the retrieval of land surface temperature from the Spin Enhanced Visible and Infrared Imager (SEVIRI) instrument over the Sahara[3] (Trigo et al., 2009). The emissivity of land tiles is adjusted in the presence of snow, reaching a value of 0.99 at complete coverage.

[3]Low emissivities over the Sahara are associated with high quartz contents. An improved approach, which might be included in the future, would be to relate the bare soil emissivity to the soil mineralogy.

Table 5. Source data used to create ozone ancillaries in the following GA3.0/3.1 and GA4.0 systems: NWP: 1–6-day NWP forecasts; MOGREPS-15: the 15-day global component of the Met Office Global and Regional Ensemble Prediction System; GloSea: the Met Office Global Seasonal forecast system; Clim: standard data set used in GA3.0 climate runs; and CMIP5: GA3.0 climate runs set up to use CMIP5 forcing data (Taylor et al., 2009).

System	GA3.0 data set	GA4.0 data set
NWP	Li and Shine (1995)	SPARC-II
MOGREPS-15	SPARC-I	SPARC-II
GloSea/Clim	Dall'Amico et al. (2010)	SPARC-II
CMIP5	SPARC-II	SPARC-II

Figure 4 shows the impact of the new emissivities on the mean clear-sky outgoing LW radiation and screen-level temperature during June–August (JJA) from a test of these tiled emissivities in a 10 yr atmosphere/land-only climate simulation at N96 resolution (approximately 135 km in the mid-latitudes). The significant reduction in the emissivity of bare soil causes a reduction in the emitted radiation over the deserts. Consequently, the surface skin and near-surface air temperatures are increased, which ameliorates a cold bias over the Middle Eastern deserts that is prominent in GA3.0/GL3.0.

In both GL3.0 and GL4.0, needle-leaved trees are represented using a canopy model that allows the snow cover to be partitioned between the canopy and the ground. In GL4.0, the parametrisation of the albedo of needle-leaved trees has been revised to make it fully consistent with this partitioning, so that the albedo is now dependent solely upon the canopy snow store.

Figure 5 shows the impact of this improved partitioning on the mean clear-sky reflected SW radiation and screen-level temperatures during March–May (MAM) in a 10 yr N96 atmosphere/land-only climate simulation. Removing the impact of snow below the canopy from the calculation of the surface albedo reduces the reflection of SW radiation over wide areas of the northern continents. This leads to a warming in excess of 1K over western Canada, which reduces a significant cold bias in this region.

Finally, a small algorithmic improvement has been made in the calculation of soil moisture fluxes. Whereas the vertical gradient of the soil suction, $\mathrm{d}\Psi/\mathrm{d}z$, was previously evaluated directly as the finite difference $\Delta\Psi/\Delta z$, in GL4.0 it has been rewritten as $\mathrm{d}\Psi/\mathrm{d}S \times \Delta S/\Delta z$, where S is the normalised water content. The former derivative is evaluated analytically and the latter as a finite difference. This calculation of $\Delta S/\Delta z$ is fully consistent with the calculation of the hydraulic conductivity at the interface between soil layers and results in better-behaved moisture fluxes in the presence of strong soil moisture gradients.

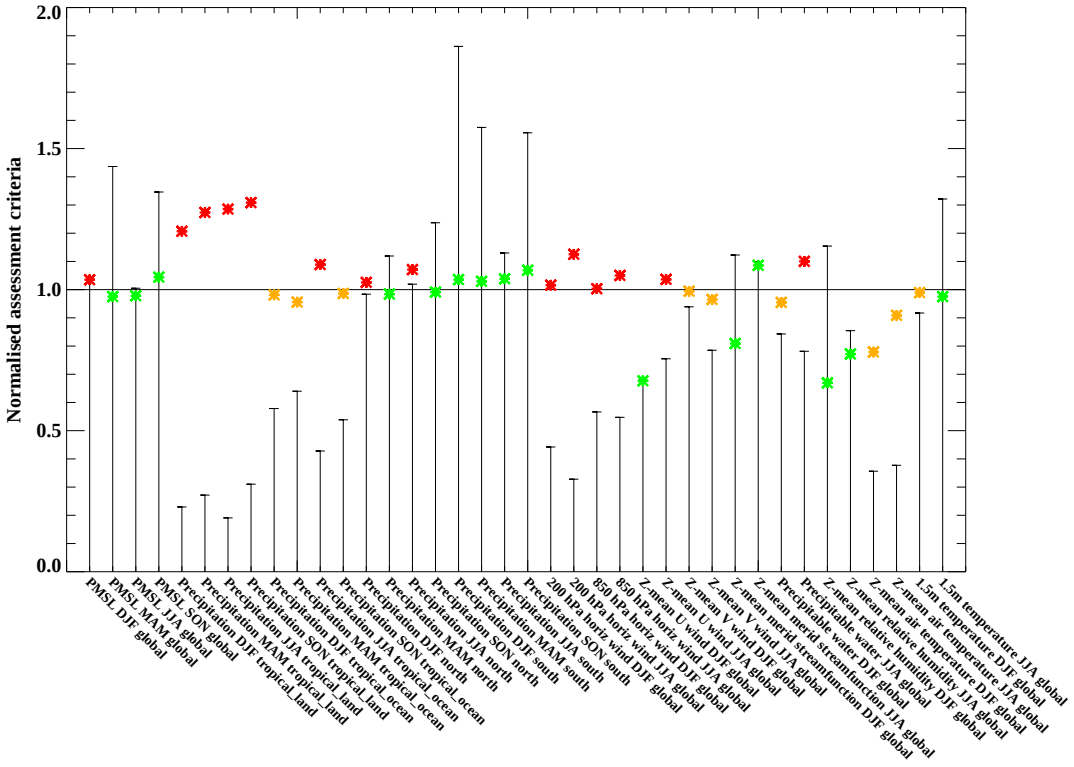

Fig. 6. Normalised assessment criteria (ratios of mean field root mean square errors) for a range of atmospheric fields from the GA4.0/GL4.0 N96-AL_clim simulation compared to a GA3.0/GL3.0 baseline. Statistics shown are from the seasons December to February (DJF), March to May (MAM), June to August (JJA) and September to November (SON) and for regions global, tropical land (land points between 30° N and 30° S), tropical ocean (ocean points between 30 °N and 30° S), north (30°–90° N) and south (30°–90° S). The observation data sets used are HadSLP2 pressure at mean sea level (Allan and Ansell, 2006), GPCP precipitation (Adler et al., 2003), SSMI precipitable water (Wentz and Spencer, 1998) and CRUTEM3 1.5 m temperature (Brohan et al., 2006), whilst the remaining climatologies are from ERA-Interim reanalyses (Berrisford et al., 2009). The whisker bars represent observational uncertainty, which is calculated by comparing the verifying data sets with alternative observations. These alternative data sets are ERA-40 pressure at mean sea level and precipitable water (Uppala et al., 2005), CMAP precipitation (Xie and Arkin, 1997), Legates and Willmott (1990) 1.5 m temperature and MERRA reanalysis (Bosilovich, 2008) for the remaining fields.

3.9 Ancillary files and forcing data

In the formulation of GA3.0, one aspect of the configuration that received less attention than others was the source data sets and processing options used in the generation of ancillary files. In GA3.0 most ancillary files were created consistently between systems when appropriate, with a few minor exceptions.

The only significant exception was the specification of atmospheric ozone (O_3), which in all systems except Earth system configurations is provided to the model as a time-varying zonal mean field via an ancillary file. The source data for these ancillaries, however, varied from system to system as tabulated in Table 5.

In GA4.0 we have moved to using the high-top version of the SPARC-II O_3 data set (Cionni et al., 2011), which was the standard data set provided for use in CMIP5 simulations. Unless otherwise required by experimental design, GA4.0 systems use an annually periodic ancillary, containing monthly means generated from SPARC-II data in the years 1994–2005.

The only other significant changes to the ancillary source data used in GA4.0 are (i) the move to deriving continuous soil properties directly from the HWSD data set (Nachtergaele et al., 2008) rather than first mapping the spatial HWSD data onto the coarse-, medium- and fine-grained soil classes of Wilson and Henderson-Sellers (1985) and (ii) the update of leaf area index data from MODIS Terra collection 4 to MODIS Terra collection 5.

4 Preliminary model evaluation

We present an initial assessment of the GA4.0/GL4.0 configurations against a GA3.0/GL3.0 control in the following systems:

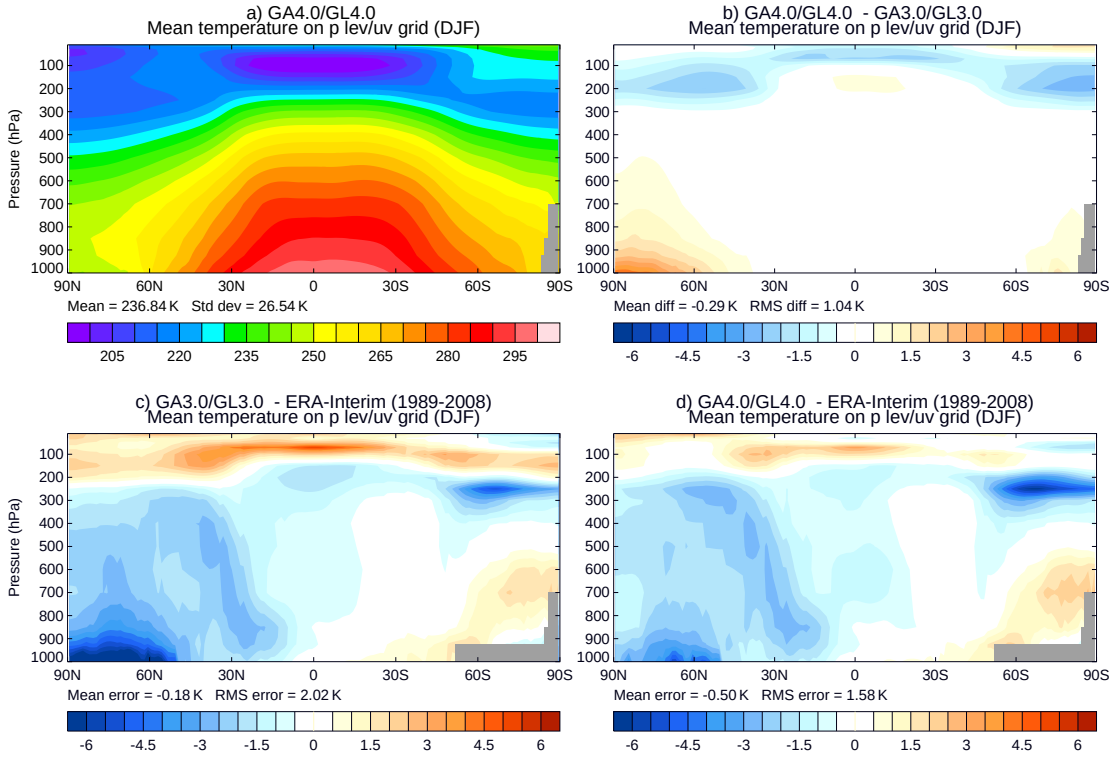

Fig. 7. Climatological zonal mean temperature field during DJF from years 11–60 of N96-AOIL_clim. **(a)** Full field from GA4.0/GL4.0, **(b)** model difference (GA4.0/GL4.0 minus GA3.0/GL3.0), **(c)** GA3.0/GL3.0 bias (GA3.0/GL3.0 minus verifying data set) and **(d)** GA4.0/GL4.0 bias (GA4.0/GL4.0 minus verifying data set). The verifying data set is the ERA-Interim reanalysis (Berrisford et al., 2009).

– N*96-AL_clim:* 25 yr (1982–2006) N96 resolution (approximately 135 km in the mid-latitudes) $L85(50_t, 35_s)_{85}$ atmosphere/land-only climate simulation using reanalysed sea-surface temperature (SST) and sea ice fields (Reynolds et al., 2007) and time-varying greenhouse gas loadings/aerosol emissions;

– N*96-AOIL_clim:* 100 yr N96 $L85(50_t, 35_s)_{85}$ atmosphere/ocean/sea ice/land current climate simulation using year 2000 greenhouse gas loadings/aerosol emissions. In this coupled system, the ocean and sea ice components use the NEMO ocean (Madec, 2008) and Los Alamos sea ice (CICE Hunke and Lipscombe, 2008) models respectively at approximately $1^\circ \times 1^\circ$ horizontal resolution. The technical infrastructure of this coupled modelling system is described in Hewitt et al. (2011);

– N*320-AL_NWP:* 2×1-month data assimilation trials of an N320 resolution (approximately 40 km in the mid-latitudes) $L70(50_t, 20_s)_{80}$ atmosphere/land-only model initialised using the Met Office 4D-Var data assimilation system (Rawlins et al., 2007) and SST and sea ice fields from OSTIA (Operational Sea-surface Temperature and sea Ice Analysis; Donlon et al., 2012). The trial periods used are 4 June–14 July 2011 and 18 January 2012–18 February 2012, with two main forecasts per day initialised at 00:00 and 12:00 UTC.

4.1 Global tropospheric assessment

Figure 6 summarises the impact of the changes described on a basic set of global circulation parameters from the N96-AL_clim simulation using normalised assessment criteria. Points show the root mean square (RMS) error of a meaned field in GA4.0/GL4.0 divided by the RMS error of the same field in GA3.0/GL3.0, with colours used to signify the relative performance of the test configuration. Amber symbols below the line (of which there are 9) show improved fields with errors that are larger than the observational uncertainty, whilst red symbols above the line (14) show fields that are degraded. Green symbols represent fields where the GA4.0/GL4.0 simulation error is within the range of observational uncertainty (whisker bars), characterised by comparing multiple data sets; this can include fields that are definitely improved, where only the test configuration are within uncertainty (in this case, 2), as well as those where both test and control lie within the whisker bars. The most significant

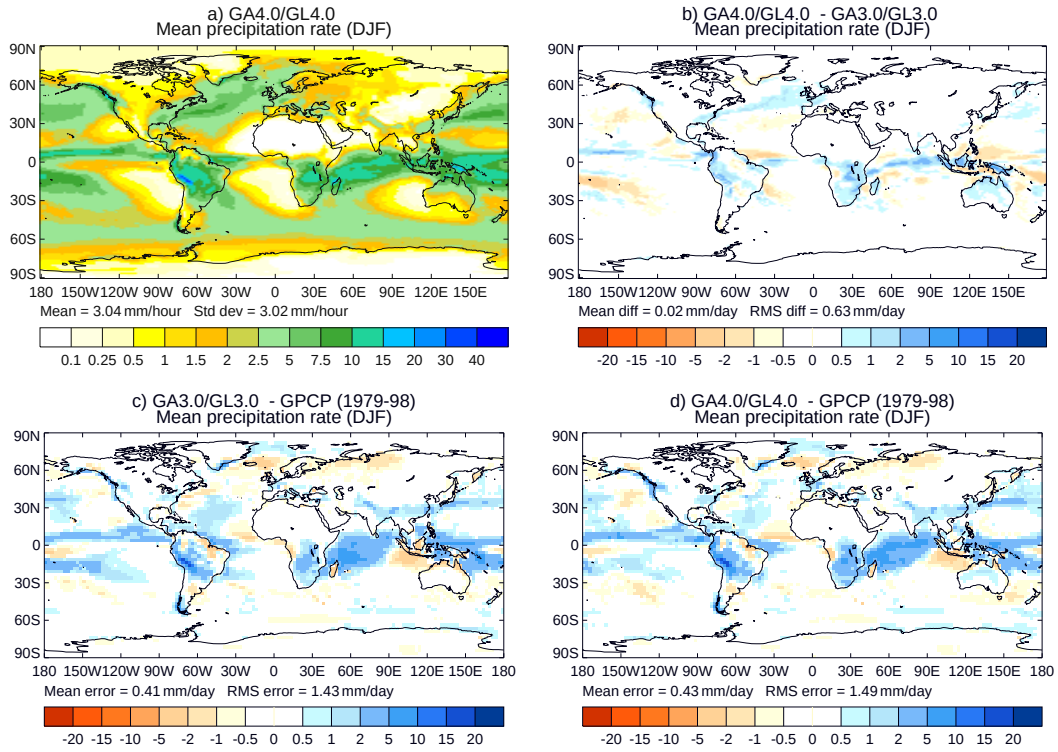

Fig. 8. Climatological mean precipitation rate during DJF from N96-AL_clim using the same format as Fig. 7. The validating data set is the GPCP climatology (Adler et al., 2003).

improvements here are in the zonal mean temperature (all year) and wind fields (December to February (DJF) only), whilst the largest detriments are in precipitation over tropical land. An equivalent plot for the N96-AOIL_clim simulation (not shown) shows the same general trends.

The main improvement to the coupled model's tropospheric climatology is the reduction in the Northern Hemisphere lower-tropospheric cold bias during DJF, which is illustrated in Fig. 7. This is due to improved near-surface temperatures over sea ice caused by the non-linear combination of a number of the science changes. The N96-AL_clim GA3.0/GL3.0 control does not exhibit such a large error in this region, where the new configuration now shows greater agreement between N96-AOIL_clim and N96-AL_clim.

The changes to convective cloud condensate and improved representation of falling ice have increased the tropospheric humidity, improving the relative humidity structure in the tropics but increasing the moist bias in the southern mid-latitudes.

4.2 Global precipitation assessment

The largest detriment in the N96-AL_clim model climatology is an increase in precipitation over tropical land regions, which has made existing wet biases worse, particularly during DJF as illustrated in Fig. 8.

We do see some improvement in precipitation biases over the ocean, however, particularly over the maritime continent in Fig. 8 and over the western Pacific warm pool in Fig. 9, which shows the equivalent fields from JJA.

The largest part of these precipitation changes has come about due to changes to the convection scheme outlined in Sect. 3.6. This package of changes was designed to improve the variability of tropical convection, but on balance this has had a detrimental impact on the mean state. The balance between these is a common dilemma in the development of atmospheric global models (e.g. see Mapes and Neale, 2011) and is an area of continuing research. This result, combined with the increase in tropical precipitation over land seen in GA3.0/GL3.0 (Walters et al., 2011), means that the improvement of tropical precipitation is something that must be prioritised during the development of future Global Atmosphere configurations.

A deficit in summer rainfall over India has been a long-standing bias in the MetUM, which is present across all timescales. Compared to the magnitude of the bias, differences between GA3.0 and GA4.0 are small. The changes made in GA4.0 were designed to encourage more convection to terminate lower down, whilst leaving the most intense convection to extend higher. This appears to have been partially successful over India, where there is a shift towards more intense, but less frequent, deep convection and more

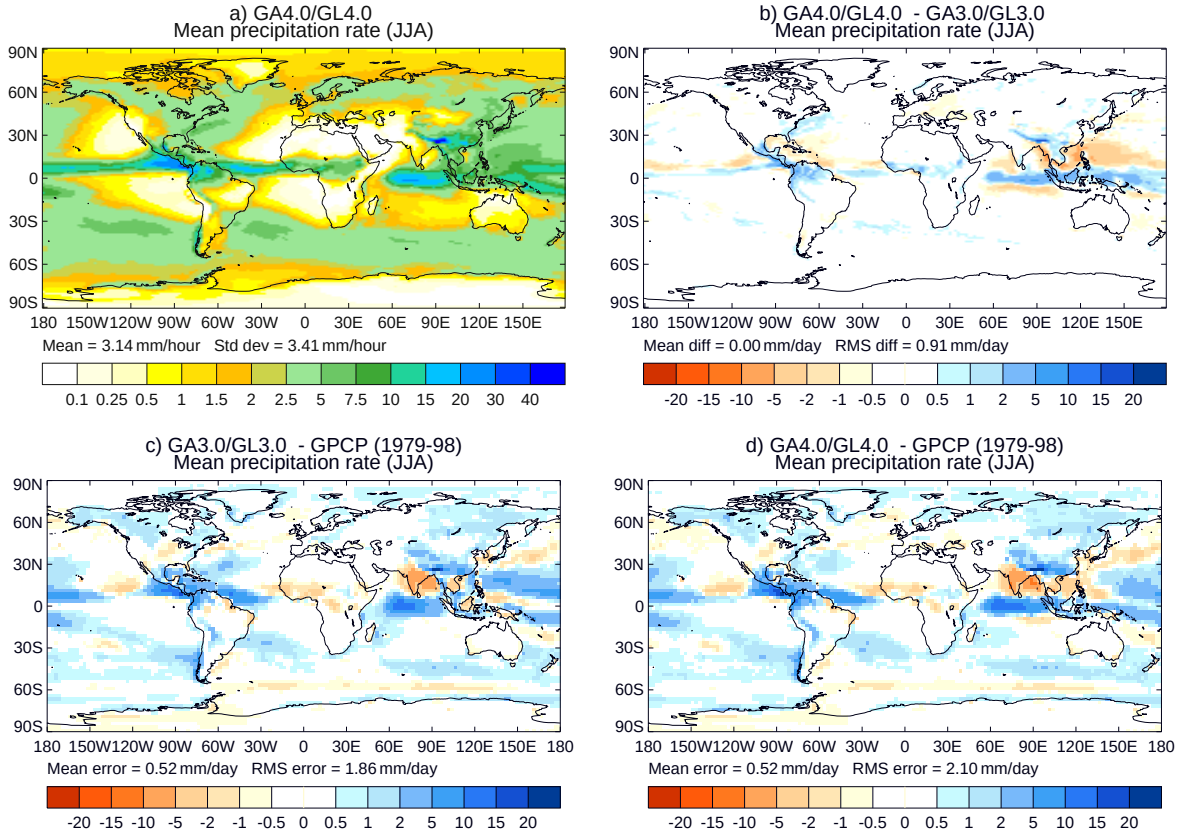

Fig. 9. Climatological mean precipitation rate during JJA from N96-AL_clim using the same format as Fig. 7.

frequent mid-level and shallow convective rain. Over the Indian Ocean, however, the more intense convection dominates, resulting in a slightly increased wet bias here and slightly larger dry bias over India. Hence, for the monsoon region, the right balance of intensities appears to be critical to avoid one region dominating over another.

One improvement in the model's precipitation characteristics that comes from the use of the Abel and Boutle (2012) drizzle particle size distribution discussed in Sect. 3.3 is a reduction in the occurrence of spurious light rain. This was a problem identified in pre-GA3.0 climate configurations and NWP configurations of the global MetUM, which was improved by the use of prognostic precipitation fields in GA3.0.

Figure 10 shows a 12 h N320-AL_NWP forecast of the instantaneous precipitation rate and pressure at mean sea level over the South Atlantic, initialised at 12:00 UTC on 10 December 2010. The plots show fields from a pre-GA3.0 physics package that was operational in the Met Office's NWP suite between July 2010 and March 2011, as well as equivalent forecasts from GA3.0 and GA4.0; please note the very low precipitation rates represented by the smallest contour intervals. This shows the widespread diagnosis of very light precipitation under the high-pressure system off the west coast of Africa, which is phenomenologically unrealistic. This is significantly reduced in GA3.0, with further smaller improvements in GA4.0 that essentially remove this undesirable feature from the model. This change also leads to an improved, increased, frequency of dry days in both N96-AOIL_clim and N96-AL_clim.

4.3 Clouds and radiation assessment

Over most parts of the world, errors in both the longwave and shortwave radiative impact of clouds have improved between GA3.0 and GA4.0.

Figure 11 shows that the clouds in N96-AL_clim are generally more reflective, whilst Fig. 12 shows that they have a larger impact on the outgoing longwave radiation. Both of these improvements are due to increases in cloud amount for a number of different cloud types resulting from the various cloud changes described in Sect. 3 such as the new cloud erosion parametrisation and the shear-dominated boundary layer change. One of the few areas where the cloud bias has increased is the eastern North Atlantic/western Europe, where not only does Fig. 11 provide evidence that there is too-much cloud in long simulations, but this is supported by NWP verification of cloud cover over a similar region as presented in Fig. 13.

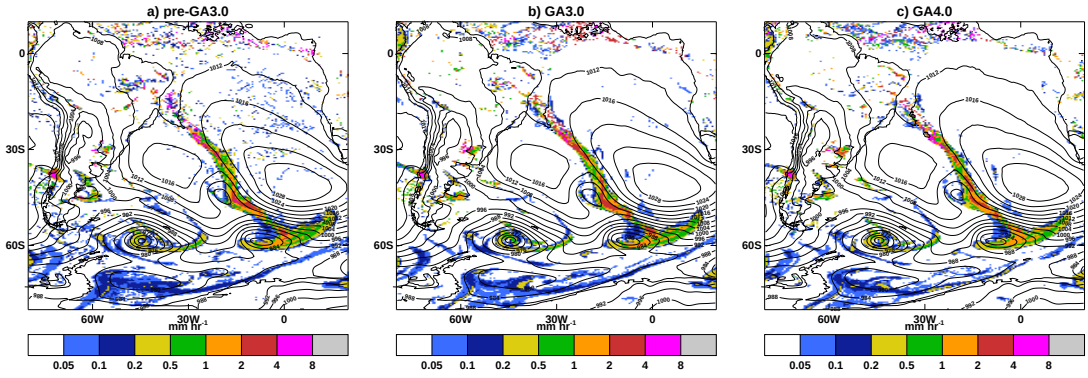

Fig. 10. A sample 24 h forecast of pressure at mean sea level (contours) and instantaneous total precipitation rate from N320-AL_NWP forecasts using a pre-GA3.0 atmospheric physics package (left), GA3.0 (centre) and GA4.0 (right).

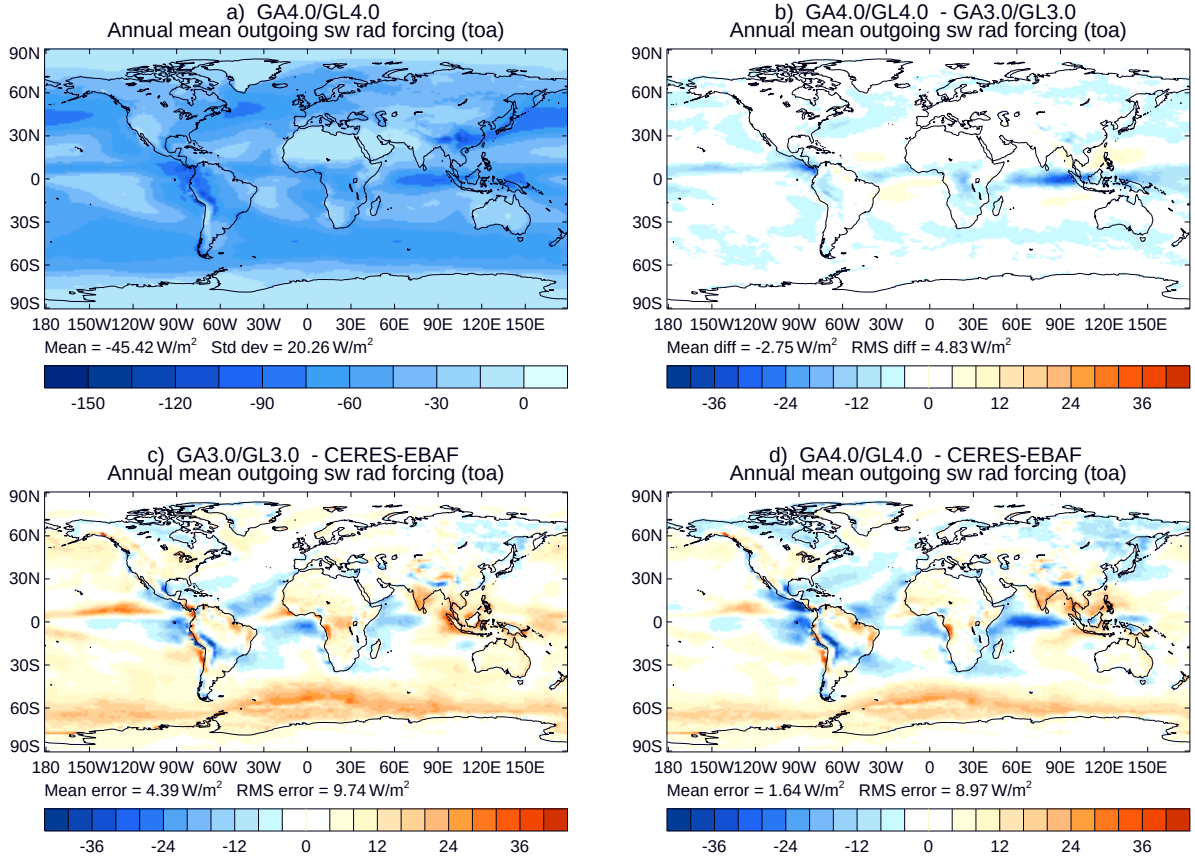

Fig. 11. Annual mean shortwave cloud forcing from N96-AL_clim using the same format as Fig. 7. The validating data set is from the CERES-EBAF climatology (Loeb et al., 2009).

A contributing factor to this error is the north–south asymmetry in the brightness of clouds, which continues to be present in GA4.0; potential contributors to this asymmetry are errors in aerosol loadings and properties, which will receive further attention in the future, particularly during the planned implementation of the UKCA-mode aerosol scheme.

4.4 Middle-atmospheric assessment

The most significant impact of GA4.0 on the middle atmosphere is a cooling in the stratosphere, which significantly reduces an existing warm bias with a maximum at about 100 hPa in the tropics. This can be seen for N96-AOIL_clim in DJF in the upper levels of Fig. 7, but a similar signal is

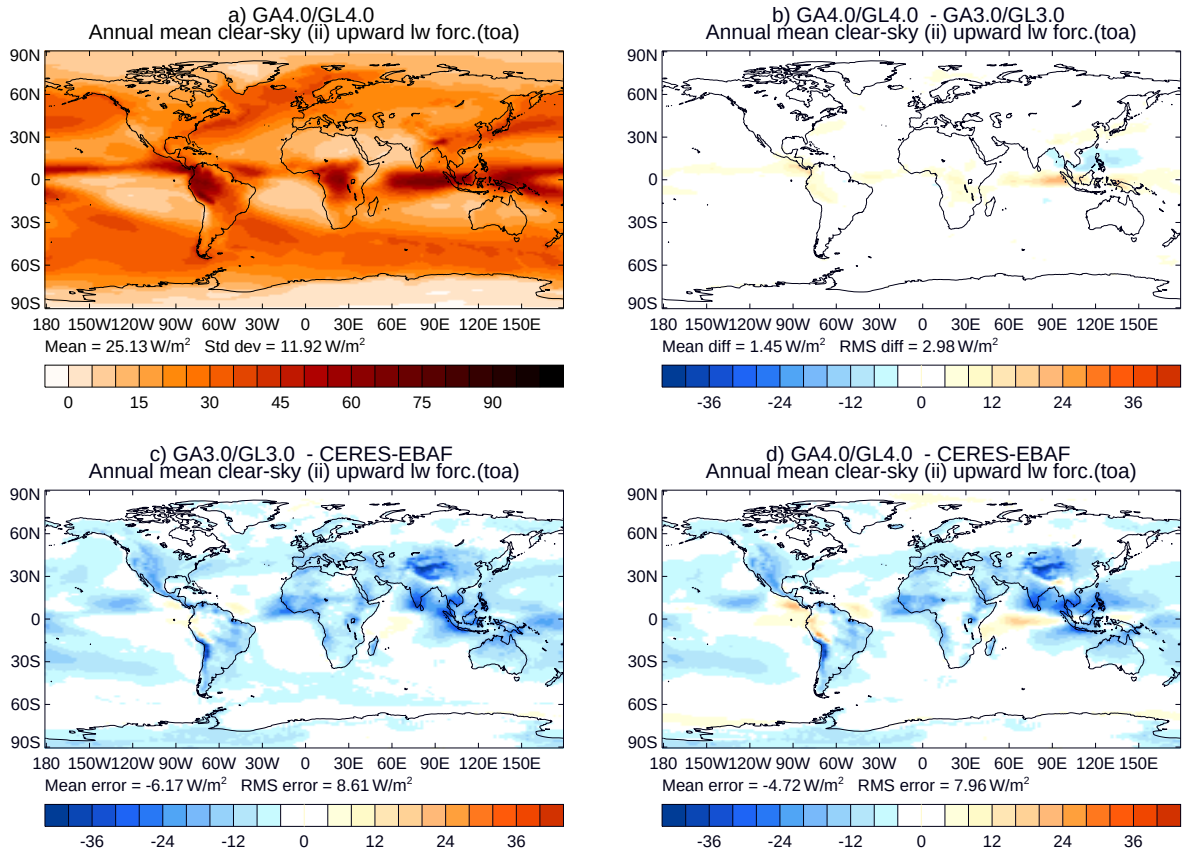

Fig. 12. Annual mean longwave cloud forcing from N96-AL_clim using the same format as Fig. 7. The validating data set is from the CERES-EBAF climatology (Loeb et al., 2009).

also seen in the other seasons as well as in N96-AL_clim (not shown). This improvement cannot be attributed to any single change described in Sect. 3, but comes from the combination of a number of these changes. There is also an improvement in upper-level temperatures in NWP simulations, which Fig. 14 shows to be particularly large in the summer hemisphere. Whilst this is due partly to the improvements seen in N96-AOIL_clim, there is a larger contribution from the replacement of the Li and Shine (1995) O_3 data set with the SPARC-II data set described in Sect. 3.9.

4.5 Problems identified with GA4.0/GL4.0

4.5.1 Global coupled precipitation – evaporation

The magnitude of the global mean precipitation minus evaporation residual has increased in the N96-AOIL_clim run from $\approx 3 \times 10^{-4}$ mm day^{-1} in GA3.0/GL3.0 to $\approx 4 \times 10^{-3}$ mm day^{-1} in GA4.0/GL4.0. This imbalance appears to have arisen from the change to using mixing ratios in the dynamics and the parallel physics, suggesting an error in some of the remaining conversions from specific quantities to mixing ratios. We have investigated and improved this in the development of GA5.0, but this error will lead to poor freshwater conservation, which makes GA4.0 unsuitable for very long coupled climate simulations.

4.5.2 Aerosol deposition errors

In the CLASSIC aerosol scheme, surface resistance to dry deposition is computed analogously to the resistance to surface heat (and moisture) exchange. In GA4.0/GL4.0, the change to the thermal roughness length for trees described in Sect. 3.8 removes the resistance from the laminar flow layer such that, over forested tiles, aerosols are deposited too easily. This has a particularly large impact on the biomass burning aerosol burden, as the majority of this aerosol is erroneously deposited soon after its emission. A short-term fix for this problem has been developed and built into GA5.0. In the longer term, the planned replacement of the CLASSIC aerosol scheme with UKCA-mode (Mann et al., 2010) will include an alternative formulation for dry deposition, improve aerosol modelling skill, and provide opportunities for new science.

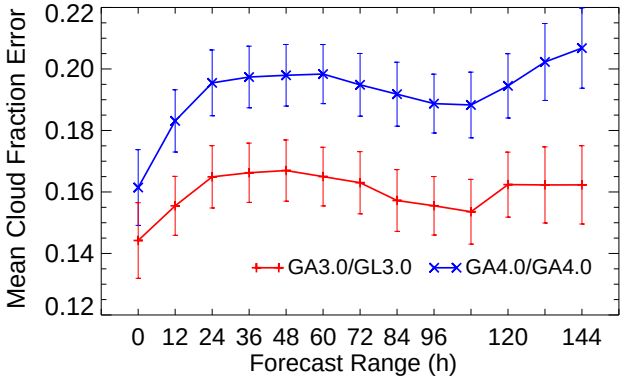

Fig. 13. Mean cloud cover forecast minus observation statistics as a function of forecast range (hours) using a mixture of manual and automatic surface observations in the North Atlantic/Europe region during the January–February N320-AL_NWP trial. This covers a rectangular area in a rotated pole projection that in standard coordinates is bounded by the points (25.5° N, 37° W), (26.5° N, 30.5° E), (57° N, 61° E) and (55.5° N, 67.5° W).

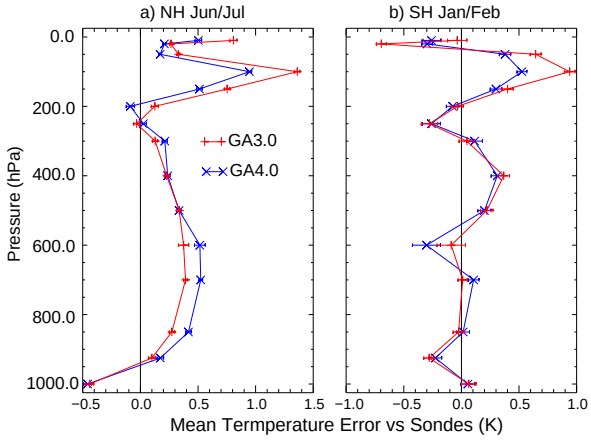

Fig. 14. Profiles of mean temperature forecast minus observation statistics from 5-day forecasts using all radiosonde observations in **(a)** the Northern Hemisphere verification area (20 °–90 ° N) during the June–July N320-AL_NWP trial and **(b)** the Southern Hemisphere verification area (20 °–90 ° S) during the January–February N320-AL_NWP trial.

5 Summary and conclusions

The 25 yr journey that the Met Office has taken towards a fully unified atmospheric modelling framework is described in Brown et al. (2012). The development of GA4.0 (and GL4.0) via the process described in Walters et al. (2011) represents another step in this direction, as this is the first time that all scientific developments have been assessed across such a wide range of systems and timescales at the same time. Both GA4.0 and GL4.0 have consolidated a number of scientific improvements into the GA and GL "trunks" and have removed some outstanding differences between NWP and climate implementations of the previous configurations.

An example of benefit from the increased scrutiny of the GA development process is best provided by a change that was not included in the final configuration: namely, the inclusion of water loading in the convection scheme. The proposed change was to include the gravitational loading of convective hydrometeors in the diagnosis and modelling of convective ascents. Initial tests showed that this significantly improved the climatology of the Indian Monsoon through the suppression of the height of deep convection over the Indian Ocean. The change was not included in the final configuration, however, as it significantly degraded the predictive skill of deterministic global NWP forecasts in the tropics. Subsequent investigations have shown that the initial formulation of this change was over-simplistic. Whilst this is still a missing process that we wish to represent in the future, a more accurate formulation is unlikely to have as large an impact on either system, which justifies our decision to withdraw this from early test configurations. This prevented us from spuriously improving the performance of the climate model in one metric through the inclusion of an inaccurately formulated process. In addition to this increased scrutiny, we have also identified areas where the process can be improved. The technical problems discussed in Sect. 4.5 were identified before we defined the final configuration, but too late in the development cycle for suitable fixes to be included. This highlights the importance of more sophisticated assessment tools for use throughout the development cycle; these have since been adopted and are proving useful in the ongoing Global Atmosphere development process.

In summary, the combined performance of GA4.0 and GL4.0 is roughly comparable to that of their predecessors. An initial assessment shows a reduced warm bias in the stratosphere and improved cloud radiative effects across most regions, although there is a degradation in the distribution of precipitation over tropical land. Performance in NWP configurations is still not sufficient to overtake the GA3.1/GL3.1 "branches" (Walters et al., 2011) used in both global deterministic and ensemble forecast systems within the Met Office's operational NWP suite. The configurations have been used, however, in several scientific investigations and sensitivity tests, and the developments made include several important improvements that will provide benefit when future configurations are implemented. We also believe that the lessons learnt in the development of GA4.0 will prove beneficial in future development cycles, which will allow us to continue developing the single scientific configuration and to achieve our goal of implementing this with no, or very limited, system-specific tunings for use across all of our global atmospheric prediction systems.

Supplementary material related to this article is available online at http://www.geosci-model-dev.net/7/361/2014/gmd-7-361-2014-supplement.pdf.

Copyright statement

Acknowledgements. A. Bodas-Salcedo, N. Bellouin, D. Copsey, C. M. Harris, S. C. Hardiman, R. C. Levine, G. M. Martin, M. D. Palmer, M. J. Roberts, J. M. Rodríguez and K. D. Williams were supported by the Joint DECC/Defra Met Office Hadley Centre Climate Programme (GA01101). The development and assessment of the Global Atmosphere/Land configurations is possible only through the hard work of a large number of people, both within and outside the Met Office, that exceeds the list of authors. We also acknowledge authors of Walters et al. (2011) who are not also authors of this paper, as parts of that publication are reproduced in Sect. 2.

Intellectual property

Due to intellectual property right restrictions, we cannot provide either the source code or documentation papers for the MetUM or JULES. The Supplement to this paper does include a set of Fortran namelists that define the configurations in the N96-AL_clim system as well as changes that should be made to use the configurations in different systems and at different horizontal resolutions.

Obtaining the MetUM

The Met Office Unified Model is available for use under licence. A number of research organisations and national meteorological services use the MetUM in collaboration with the Met Office to undertake basic atmospheric process research, produce forecasts, develop the MetUM code and build and evaluate Earth system models. For further information on how to apply for a licence see http://www.metoffice.gov.uk/research/collaboration/um-collaboration.

Obtaining JULES

JULES is available under licence free of charge. For further information on how to gain permission to use JULES for research purposes see https://jules.jchmr.org/software-and-documentation.

Edited by: D. Ham

References

Abel, S. J. and Boutle, I. A.: An improved representation of the raindrop size distribution for single-moment microphysics schemes, Q. J. Roy. Meteorol. Soc., 138, 2151–2162, doi:10.1002/qj.1949, 2012.

Abel, S. J. and Shipway, B. J.: A comparison of cloud-resolving model simulations of trade wind cumulus with aircraft observations taken during RICO, Q. J. Roy. Meteorol. Soc., 133, 781–794, doi:10.1002/qj.55, 2007.

Abel, S. J., Walters, D. N., and Allen, G.: Evaluation of stratocumulus cloud prediction in the Met Office forecast model during VOCALS-REx, Atmos. Chem. Phys., 10, 10541–10559, doi:10.5194/acp-10-10541-2010, 2010.

Adler, R. F., Huffman, G. J., Chang, A., Ferraro, R., Xie, P.-P., Janowiak, J., Rudolf, B., Schneider, U., Curtis, S., Bolvin, D., Gruber, A., Susskind, J., Arkin, P., and Nelkin, E.: The version-2 Global Precipitation Climatology Project (GPCP) monthly precipitation analysis (1979–present), J. Hydrometeor., 4, 1147–1167, doi:10.1175/1525-7541(2003)004<1147:TVGPCP>2.0.CO;2, 2003.

Allan, R. and Ansell, T.: A new globally complete monthly historical gridded mean sea level pressure dataset (HadSLP2): 1850–2004, J. Climate, 19, 5816–5842, doi:10.1175/JCLI3937.1, 2006.

Anderson, P. S.: Measurement of Prandtl Number as a Function of Richardson Number Avoiding Self-Correlation, Bound.-Lay.Meteorol., 131, 345–362, doi:10.1007/s10546-009-9376-4, 2009.

Andreas, E. L.: A theory for the scalar roughness and the scalar transfer coefficients over snow and sea ice, Bound.-Lay. Meteorol., 38, 159–184, doi:10.1007/BF00121562, 1987.

Andreas, E. L., Horst, T. W., Grachev, A. A., Persson, P. O. G., Fairall, C. W., Guest, P. S., and Jordan, R. E.: Parametrizing turbulent exchange over summer sea ice and the marginal ice zone, Q. J. R. Meteorol. Soc., 136, 927–943, doi:10.1002/qj.618, 2010.

Andres, R. J. and Kasgnoc, A. D.: A time-averaged inventory of subaerial volcanic sulfur emissions, J. Geophys. Res., 103, 25251–25261, doi:10.1029/98JD02091, 1998.

Arakawa, A. and Lamb, V. R.: Computational design of the basic dynamic processes of the UCLA general circulation model, Methods Comput. Phys., 17, 173–265, 1977.

Barker, H. W. and Li, Z.: Improved simulation of clear-sky shortwave radiative transfer in the CCC-GCM, J. Climate, 8, 2213–2223, doi:10.1175/1520-0442(1995)008<2213:ISOCSS>2.0.CO;2, 1995.

Beare, R. J., MacVean, M. K., Holtslag, A. A. M., Cuxart, J., Esau, I., Golaz, J.-C., Jimenez, M. A., Khairoutdinov, M., Kosovic, B., Lewellen, D., Lund, T. S., Lundquist, J. K., McCabe, A., Moene, A. F., Noh, Y., Raasch, S., and Sullivan, P.: An intercomparison of large-eddy simulations of the stable boundary layer., Bound.-Lay. Meteorol., 118, 247–272, 2006.

Beljaars, A. C. M. and Holtslag, A. A. M.: Flux parametrization over land surfaces for atmospheric models, J. Appl. Meteorol., 30, 327–341, doi:10.1175/1520-0450(1991)030<0327:FPOLSF>2.0.CO;2, 1991.

Bellouin, N., Rae, J., Jones, A., Johnson, C., Haywood, J., and Boucher, O.: Aerosol forcing in the Climate Model Intercomparison Project (CMIP5) simulations by HadGEM2-ES and the role of ammonium nitrate, J. Geophys. Res., 116, D20206, doi:10.1029/2011JD016074, 2011.

Berrisford, P., Dee, D., Fielding, K., Fuentes, M., Kållberg, P., Kobayashi, S., and Uppala, S.: The ERA-Interim archive, Tech. Rep. 1, ERA report series, ECMWF, Reading, UK, 2009.

Best, M. J.: Representing urban areas within operational numerical weather prediction models, Bound.-Lay. Meteorol., 114, 91–109, doi:10.1007/s10546-004-4834-5, 2005.

Best, M. J., Pryor, M., Clark, D. B., Rooney, G. G., Essery, R. L. H., Ménard, C. B., Edwards, J. M., Hendry, M. A., Porson, A.,

Gedney, N., Mercado, L. M., Sitch, S., Blyth, E., Boucher, O., Cox, P. M., Grimmond, C. S. B., and Harding, R. J.: The Joint UK Land Environment Simulator (JULES), model description – Part 1: Energy and water fluxes, Geosci. Model Dev., 4, 677–699, doi:10.5194/gmd-4-677-2011, 2011.

Beven, K. J. and Kirkby, M. J.: A physically based, variable contributing area model of basin hydrology, Hydrol. Sci. Bull., 24, 43–69, doi:10.1080/02626667909491834, 1979.

Birch, C. E., Brooks, I. M., Tjernström, M., Milton, S. F., amd S. Söderberg, P. E., and Persson, P. O. G.: The performance of a global and mesoscale model over the central Arctic Ocean during late summer, J. Geophys. Res., 114, D13104, doi:10.1029/2008JD010790, 2009.

Bodas-Salcedo, A., Williams, K. D., Field, P. R., and Lock, A. P.: The surface downwelling solar radiation surplus over the Southern Ocean in the Met Office model: the role of midlatitude cyclone clouds, J. Climate, 25, 7467–7486, doi:10.1175/JCLI-D-11-00702.1, 2012.

Bosilovich, M. G.: NASA's modern era retrospective-analysis for research and applications: Integrating Earth observations, Earthzine, available at: http://www.earthzine.org/2008/09/26/nasas-modern-era-retrospective-analysis (last access: 30 November 2013), 2008.

Brohan, P., Kennedy, J. J., Harris, I., Tett, S. F. B., and Jones, P. D.: Uncertainty estimates in regional and global observed temperature changes: a new dataset from 1850, J. Geophys. Res., 111, D12106, doi:10.1029/2005JD006548, 2006.

Brown, A. R.: Large-eddy simulation and parametrization of the baroclinic boundary-layer, Q. J. Roy. Meteorol. Soc., 122, 1779–1798, doi:10.1002/qj.49712253603, 1996.

Brown, A. R., Milton, S., Cullen, M., Golding, B., Mitchell, J., and Shelly, A.: Unified modeling and prediction of weather and climate: a 25 year journey, Bull. Am. Meteorol. Soc., 93, 1865–1877, doi:10.1175/BAMS-D-12-00018.1, 2012.

Brown, A. R. and Webster, S.: Orographic flow-blocking scheme characteristics, Q. J. Roy. Meteorol. Soc., 130, 3015–3028, doi:10.1256/qj.04.40, 2004.

Brown, A. R., Beare, R. J., Edwards, J. M., Lock, A. P., Keogh, S. J., Milton, S. F., and Walters, D. N.: Upgrades to the boundary-layer scheme in the Met Office numerical weather prediction model, Bound.-Lay. Meteorol., 128, 117–132, doi:10.1007/s10546-008-9275-0, 2008.

Bush, S. J., Turner, A. G., Woolnough, S., and Martin, G.: The Effect of an Increased Convective Entrainment Rate on Indian Monsoon Biases in the Met Office Unified Model, Poster presented at AGU Fall Meeting, San Francisco, USA, 3–7 December, 2012, available at: http://fallmeeting.agu.org/2012/files/2012/12/agu_2012_final.pdf (last access: 16 January 2013), 2012.

Bushell, A. C., Wilson, D. R., and Gregory, D.: A description of cloud production by non-uniformly distributed processes, Q. J. Roy. Meteorol. Soc., 129, 1435–1455, doi:10.1256/qj.01.110, 2003.

Charney, J. G. and Phillips, N. A.: Numerical integration of the quasi-geostrophic equations for barotropic and simple baroclinic flows, J. Meteor., 10, 71–99, doi:10.1175/1520-0469(1953)010<0071:NIOTQG>2.0.CO;2, 1953.

Chen, F. and Zhang, Y.: On the coupling strength between the land surface and the atmosphere: From viewpoint of surface exchange coefficients, Geophys. Res. Lett., 36, L10404, doi:10.1029/2009GL037980, 2009.

Cionni, I., Eyring, V., Lamarque, J. F., Randel, W. J., Stevenson, D. S., Wu, F., Bodeker, G. E., Shepherd, T. G., Shindell, D. T., and Waugh, D. W.: Ozone database in support of CMIP5 simulations: results and corresponding radiative forcing, Atmos. Chem. Phys., 11, 11267–11292, doi:10.5194/acp-11-11267-2011, 2011.

Clark, D. B., Mercado, L. M., Sitch, S., Jones, C. D., Gedney, N., Best, M. J., Pryor, M., Rooney, G. G., Essery, R. L. H., Blyth, E., Boucher, O., Harding, R. J., Huntingford, C., and Cox, P. M.: The Joint UK Land Environment Simulator (JULES), model description – Part 2: Carbon fluxes and vegetation dynamics, Geosci. Model Dev., 4, 701–722, doi:10.5194/gmd-4-701-2011, 2011.

Clough, S. A., Kneizys, F. X., and Davies, R. W.: Line shape and the water vapor continuum, Atmos. Res., 23, 229–241, doi:10.1016/0169-8095(89)90020-3, 1989.

Cox, P.: Description of the TRIFFID dynamic global vegetation model, Tech. Rep. 24, Hadley Centre, Met Office, Bracknell, UK, 2001.

Cox, P. M., Betts, R. A., Bunton, C. B., Essery, R., Rowntree, P. R., and Smith, J.: The impact of new land surface physics on the GCM simulation of climate and climate sensitivity, Clim. Dynam., 15, 183–203, doi:10.1007/s003820050276, 1999.

Cox, P. M., Betts, R. A., Jones, C. D., Spall, S. A., and Totterdell, I. J.: Acceleration of global warming due to carbon-cycle feedbacks in a coupled climate model, Nature, 408, 18–187, doi:10.1038/35041539, 2000.

Cullen, M. J. P.: The unified forecast/climate model, Meteor. Mag., 122, 81–94, 1993.

Cusack, S., Slingo, A., Edwards, J. M., and Wild, M.: The radiative impact of a simple aerosol climatology on the Hadley Centre atmospheric GCM, Q. J. Roy. Meteorol. Soc., 124, 2517–2526, doi:10.1002/qj.49712455117, 1998.

Cusack, S., Edwards, J. M., and Crowther, J. M.: Investigating *k* distribution methods for parameterizing gaseous absorption in the Hadley Centre climate model, J. Geophys. Res., 104, 2051–2057, doi:10.1029/1998JD200063, 1999.

Dall'Amico, M., Gray, L. J., Rosenlof, K. H., Scaife, A. A., Shine, K. P., and Stott, P. A.: Stratospheric temperature trends: impact of ozone variability and the QBO, Clim. Dynam., 34, 381–398, doi:10.1007/s00382-009-0604-x, 2010.

Davies, T., Cullen, M. J. P., Malcolm, A. J., Mawson, M. H., Staniforth, A., White, A. A., and Wood, N.: A new dynamical core for the Met Office's global and regional modelling of the atmosphere, Q. J. Roy. Meteorol. Soc., 131, 1759–1782, doi:10.1256/qj.04.101, 2005.

Derbyshire, S. H., Maidens, A. V., Milton, S. F., Stratton, R. A., and Willett, M. R.: Adaptive detrainment in a convective parametrization, Quart. J. Roy. Meteorol. Soc., 137, 1856–1871, doi:10.1002/qj.875, 2011.

Derwent, R. G., Collins, W. J., Jenkin, M. E., Johnson, C. E., and Stevenson, D. S.: The global distribution of secondary particulate matter in a 3-D Lagrangian chemistry transport model, J. Atmos. Chem, 44, 57–95, doi:10.1023/A:1022139814102, 2003.

Dharssi, I., Vidale, P. L., Verhoef, A., Macpherson, B., Jones, C., and Best, M.: New soil physical properties implemented in the Unified Model at PS18, Tech. Rep. 528, Forecasting R&D, Met Office, Exeter, UK, 2009.

Donlon, C. J., Martin, M., Stark, J. D., Roberts-Jones, J., Fiedler, E., and Wimmer, W.: The Operational Sea Surface Temperature and Sea Ice Analysis (OSTIA) system, Remote Sens. Environ., 116, 140–158, doi:10.1016/j.rse.2010.10.017, 2012.

Dyer, A. J. and Hicks, B. B.: Flux-gradient relationships in the constant flux layer, Q. J. Roy. Meteorol. Soc., 96, 715–721, doi:10.1002/qj.49709641012, 1970.

Edwards, J. M.: Efficient calculation of infrared fluxes and cooling rates using the two-stream equations, J. Atmos. Sci., 53, 1921–1932, doi:10.1175/1520-0469(1996)053<1921:ECOIFA>2.0.CO;2, 1996.

Edwards, J. M. and Slingo, A.: Studies with a flexible new radiation code, I: Choosing a configuration for a large-scale model, Q. J. Roy. Meteorol. Soc., 122, 689–719, 1996.

Edwards, J. M., Havemann, S., Thelen, J.-C., and Baran, A. J.: A new parametrization for the radiative properties of ice crystals: Comparison with existing schemes and impact in a GCM, Atmos. Res., 83, 19–35, 2007.

Essery, R. L. H., Best, M. J., Betts, R. A., Cox, P. M., and Taylor, C. M.: Explicit representation of subgrid heterogeneity in a GCM land surface scheme, J. Hydrometeor., 4, 530–543, doi:10.1175/1525-7541(2003)004<0530:EROSHI>2.0.CO;2, 2003.

Falloon, P. D. and Betts, R. A.: The impact of climate change on global river flow in HadGEM1 simulations, Atmos. Sci. Lett., 7, 62–68, 2006.

Falloon, P. D., Betts, R., Wiltshire, A., Dankers, R., Mathison, C., McNeall, D., Bates, P., and Trigg, M.: Validation of river flows in HadGEM1 and HadCM3 with the TRIP river flow model, J. Hydrometeor., 12, 1157–1180, doi:10.1175/2011JHM1388.1, 2011.

Field, P. R., Cotton, R. J., McBeath, K., Lock, A. P., Webster, S., and Allan, R. P.: Improving a convection permitting model simulation of a cold air outbreak, Q. J. Roy. Meteorol. Soc., doi:10.1002/qj.2116, online first, 2013.

Fritsch, J. M. and Chappell, C. F.: Numerical prediction of convectively driven mesoscale pressure systems. Part I: convective parameterization, J. Atmos. Sci., 37, 1722–1733, doi:10.1175/1520-0469(1980)037<1722:NPOCDM>2.0.CO;2, 1980.

Gedney, N. and Cox, P. M.: The sensitivity of global climate model simulations to the representation of soil moisture heterogeneity, J. Hydrometeor., 4, 1265–1275, doi:10.1175/1525-7541(2003)004<1265:TSOGCM>2.0.CO;2, 2003.

Global Soil Data Task: Global soil data products CD-ROM (IGBP-DIS), CD-ROM, International Geosphere-Biosphere Programme, Data and Information System, Potsdam, Germany. Available from Oak Ridge National Laboratory Distributed Active Archive Center, Oak Ridge, TN, available at: http://www.daac.ornl.gov (last access: 30 November 2013), 2000.

Godfrey, J. S. and Beljaars, A. C. M.: On the turbulent fluxes of buoyancy, heat and moisture at the air-sea interface at low wind speeds, J. Geophys. Res., 96, 22043–22048, doi:10.1029/91JC02015, 1991.

Grant, A. L. M.: Cloud-base fluxes in the cumulus-capped boundary layer, Q. J. Roy. Meteorol. Soc., 127, 407–421, doi:10.1002/qj.49712757209, 2001.

Grant, A. L. M. and Brown, A. R.: A similarity hypothesis for shallow-cumulus transports, Q. J. Roy. Meteorol. Soc., 125, 1913–1936, 1999.

Greeley, R., Blumberg, D. G., McHone, J. F., Dobrovolskis, A., Iversen, J. D., Lancaster, N., Rasmussen, K. R., Wall, S. D., and White, B. R.: Applications of spaceborne radar laboratory data to the study of aeolian processes, J. Geophys. Res., 102, 10971–10983, doi:10.1029/97JE00518, 1997.

Gregory, D. and Allen, S.: The effect of convective downdraughts upon NWP and climate simulations, in: Ninth conference on numerical weather prediction, Denver, Colorado, 122–123, 1991.

Gregory, D. and Rowntree, P. R.: A massflux convection scheme with representation of cloud ensemble characteristics and stability dependent closure, Mon. Weather Rev., 118, 1483–1506, doi:10.1175/1520-0493(1990)118<1483:AMFCSW>2.0.CO;2, 1990.

Gregory, D., Kershaw, R., and Inness, P. M.: Parametrization of momentum transport by convection II: Tests in single-column and general circulation models, Q. J. Roy. Meteorol. Soc., 123, 1153–1183, doi:10.1002/qj.49712354103, 1997.

Gregory, D., Shutts, G. J., and Mitchell, J. R.: A new gravity-wave-drag scheme incorporating anisotropic orography and low-level wave breaking: Impact upon the climate of the UK Meteorological Office Unified Model, Q. J. Roy. Meteorol. Soc., 124, 463–493, doi:10.1002/qj.49712454606, 1998.

Hastings, D. A., Dunbar, P. K., Elphingstone, G. M., Bootz, M., Murakami, H., Maruyama, H., Masaharu, H., Holland, P., Payne, J., Bryant, N. A., Logan, T. L., Muller, J.-P., Schreier, G., and MacDonald, J. S.: The Global Land One-kilometer Base Elevation (GLOBE) Digital Elevation Model, Version 1.0, Digital data base on the World Wide Web, available at: http://www.ngdc.noaa.gov/mgg/topo/globe.html (last access: 30 November 2013), 1999.

Hewitt, H. T., Copsey, D., Culverwell, I. D., Harris, C. M., Hill, R. S. R., Keen, A. B., McLaren, A. J., and Hunke, E. C.: Design and implementation of the infrastructure of HadGEM3: the next-generation Met Office climate modelling system, Geosci. Model Dev., 4, 223–253, doi:10.5194/gmd-4-223-2011, 2011.

Hill, P. G., Manners, J., and Petch, J. C.: Reducing noise associated with the Monte Carlo Independent Column Approximation for weather forecasting models, Q. J. Roy. Meteorol. Soc., 137, 219–228, doi:10.1002/qj.732, 2011.

Hunke, E. C. and Lipscombe, W. H.: CICE: the Los Alamos sea ice model documentation and software user's manual, Version 4.0, LA-CC-06-012, Los Alamos National Laboratory, New Mexico, 2008.

Johansen, O.: Thermal conductivity of soils, Ph.D. thesis, University of Trondheim, Norway, 1975.

Jones, A., Roberts, D. L., and Slingo, A.: A climate model study of indirect radiative forcing by anthropogenic sulphate aerosols, Nature, 370, 450–453, doi:10.1038/370450a0, 1994.

Jones, A., Roberts, D. L., Woodage, M. J., and Johnson, C. E.: Indirect sulphate aerosol forcing in a climate model with an interactive sulphur cycle, J. Geophys. Res., 106, 20293–20310, doi:10.1029/2000JD000089, 2001.

Kettle, A. J., Andreae, M. O., Amouroux, D., Andreae, T. W., Bates, T. S., Berresheim, H., Bingemer, H., Boniforti, R., Curran, M. A. J., DiTullio, G. R., Helas, G., Jones, G. B., Keller, M. D., Kiene, R. P., Leck, C., Levasseur, M., Malin, G., Maspero, M., Matrai, P., M., A. R., M., N., N., C., B., Novo, A., Putaud, J. P., Rapsomanikis, S., Roberts, G., Schebeske, G., Sharma, S., Simó, R., Staubes, R., Turner, S., and Uher, G.: A global database of sea surface dimethyl sulfide (DMS) measurements and a pro-

cedure to predict sea surface DMS as a function of latitude, longitude, and month, Global Biogeochem. Cy., 13, 399–444, doi:10.1029/1999GB900004, 1999.

Klingaman, N. P. and Woolnough, S. J.: Using a case-study approach to improve the Madden-Julian oscillation in the Hadley Centre model, Q. J. Roy. Meteorol. Soc., submitted, 2013.

Kurucz, R. L. and Bell, B.: Atomic Line Data, CD-ROM 23, Harvard Smithsonian Center for Astrophysics, Cambridge, MA, 1995.

Lamarque, J.-F., Bond, T. C., Eyring, V., Granier, C., Heil, A., Klimont, Z., Lee, D., Liousse, C., Mieville, A., Owen, B., Schultz, M. G., Shindell, D., Smith, S. J., Stehfest, E., Van Aardenne, J., Cooper, O. R., Kainuma, M., Mahowald, N., McConnell, J. R., Naik, V., Riahi, K., and van Vuuren, D. P.: Historical (1850–2000) gridded anthropogenic and biomass burning emissions of reactive gases and aerosols: methodology and application, Atmos. Chem. Phys., 10, 7017–7039, doi:10.5194/acp-10-7017-2010, 2010..

Laurent, B., Marticorena, B., Bergametti, G., Chazette, P., Maignan, F., and Schmechtig, C.: Simulation of the mineral dust emission frequencies from desert areas of China and Mongolia using an aerodynamic roughness length map derived from the POLDER/ADEOS 1 surface products, J. Geophys. Res., 110, D18S04, doi:10.1029/2004JD005013, 2005.

Lean, J.: Evolution of the Sun's spectral irradiance since the Maunder Minimum, Geophys. Res. Lett., 27, 2425–2428, doi:10.1029/2000GL000043, 2000.

Legates, D. R. and Willmott, C. J.: Mean seasonal and spatial variability in global surface air temperature, Theor. Appl. Climatol., 41, 11–21, doi:10.1007/BF00866198, 1990.

Li, D. and Shine, K. P.: A 4-Dimensional Ozone Climatology for UGAMP Models, Tech. Rep. 35, UGAMP, 1995.

Lock, A. P.: The numerical representation of entrainment in parametrizations of boundary layer turbulent mixing, Mon. Weather Rev., 129, 1148–1163, doi:10.1175/1520-0493(2001)129<1148:TNROEI>2.0.CO;2, 2001.

Lock, A. P., Brown, A. R., Bush, M. R., Martin, G. M., and Smith, R. N. B.: A new boundary layer mixing scheme, Part I: Scheme description and single-column model tests, Mon. Weather Rev., 128, 3187–3199, doi:10.1175/1520-0493(2000)128<3187:ANBLMS>2.0.CO;2, 2000.

Loeb, N. G., Wielicki, B. A., Doelling, D. R., Smith, G. L., Keyes, D. F., Kato, S., Manalo-Smith, N., and Wong, T.: Toward Optimal Closure of the Earth's Top-of-Atmosphere Radiation Budget, J. Climate, 22, 748–766, doi:10.1175/2008JCLI2637.1, 2009.

Madec, G.: NEMO ocean engine, Institut Piere-Simon Laplace (IPSL), France, No. 27, ISSN No. 1288–1619, 2008.

Mann, G. W., Carslaw, K. S., Spracklen, D. V., Ridley, D. A., Manktelow, P. T., Chipperfield, M. P., Pickering, S. J., and Johnson, C. E.: Description and evaluation of GLOMAP-mode: a modal global aerosol microphysics model for the UKCA composition-climate model, Geosci. Model Dev., 3, 519–551, doi:10.5194/gmd-3-519-2010, 2010.

Manners, J., Thelen, J.-C., Petch, J., Hill, P., and Edwards, J. M.: Two fast radiative transfer methods to improve the temporal sampling of clouds in numerical weather prediction and climate models, Q. J. Roy. Meteorol. Soc., 135, 457–468, doi:10.1002/qj.956, 2009.

Manners, J., Vosper, S. B., and Roberts, N.: Radiative transfer over resolved topographic features for high-resolution weather prediction, Q. J. Roy. Meteorol. Soc., 138, 720–733, doi:10.1002/qj.956, 2012.

Mapes, B. and Neale, R.: Parameterizing convective organization, J. Adv. Model. Earth Syst., 3, M06004, doi:10.1029/2011MS000042, 2011.

Martin, G. M., Milton, S. F., Senior, C. A., Brooks, M. E., Ineson, S., Reichler, T., and Kim, J.: Analysis and reduction of systematic errors through a seamless approach to modeling weather and climate, J. Climate, 23, 5933–5957, doi:10.1175/2010JCLI3541.1, 2010.

McCabe, A. and Brown, A. R.: The role of surface heterogeneity in modelling the stable boundary layer, Bound.-Lay. Meteorol., 122, 517–534, doi:10.1007/s10546-006-9119-8, 2007.

Mercado, L. M., Huntingford, C., Gash, J. H. C., Cox, P. M., and Jogireddy, V.: Improving the representation of radiative interception and photosynthesis for climate model applications, Tellus, B59, 553–565, doi:10.1111/j.1600-0889.2007.00256.x, 2007.

Mlawer, E. J., Clough, S. A., Brown, P. D., and Tobin, D. C.: Recent developments in the water vapor continuum, in: Ninth ARM Science Team meeting, San Antonio, Texas, 22–26 March 1999, edited by: Burleigh, N. and Carrothers, D., 1–6, 1999.

Mölder, M. and Lindroth, A.: Thermal roughness length of a boreal forest, Agr. Forest Meteorol., 98–99, 659–670, 1999.

Morcrette, C. J.: Improvements to a prognostic cloud scheme through changes to its cloud erosion parametrization, Atmos. Sci. Lett., 13, 95–102, doi:10.1002/asl.374, 2012.

Morcrette, C. J. and Petch, J. C.: Analysis of prognostic cloud scheme increments in a climate model, Q. J. Roy. Meteorol. Soc., 136, 2061–2073, doi:10.1002/qj.720, 2010.

Nachtergaele, F., van Velthuizen, H., Verelst, L., Batjes, N., Dijkshoorn, K., van Engelen, V., Fischer, G., Jones, A., Montanarella, L., Petri, M., Prieler, S., Teixeira, E., Wiberg, D., and Shi, X.: Harmonized World Soil Database (version 1.0), FAO, Rome, Italy and IIASA, Laxenburg, Austria, 2008.

Nicholls, S.: The dynamics of stratocumulus: Aircraft observations and comparisons with a mixed layer model, Q. J. Roy. Meteorol. Soc., 110, 783–820, doi:10.1002/qj.49711046603, 1984.

Oki, T.: Validating the runoff from LSP-SVAT models using a global river routing network by one degree mesh, in: AMS 13th Conference on Hydrology, Long Beach, California, 2–7 February 1997, 319–322, 1997.

Oki, T. and Sud, Y. C.: Design of Total Runoff Integrating Pathways (TRIP) — A global river channel network, Earth Interact., 2, 1–36, doi:10.1175/1087-3562(1998)002<0001:DOTRIP>2.3.CO;2, 1998.

Posselt, R. and Lohmann, U.: Introduction of prognostic rain in ECHAM5: design and single column model simulations, Atmos. Chem. Phys., 8, 2949–2963, doi:10.5194/acp-8-2949-2008, 2008.

Rawlins, F., Ballard, S. P., Bovis, K. J., Clayton, A. M., Li, D., Inverarity, G. W., Lorenc, A. C., and Payne, T. J.: The Met Office global four-dimensional variational data assimilation scheme, Q. J. Roy. Meteorol. Soc., 133, 347–362, doi:10.1002/qj.32, 2007.

Redelsperger, J.-L., Guichard, F., and Mondon, S.: A parametrization of mesoscale enhancement of surface fluxes for large-scale models, J. Climate, 13, 402–421, doi:10.1175/1520-0442(2000)013<0402:APOMEO>2.0.CO;2, 2000.

Reynolds, R. W., Smith, T. M., Liu, C., Chelton, D. B., Casey, K. S., and Schlax, M. G.: Daily High-Resolution-Blended Analyses for Sea Surface Temperature, J. Climate, 20, 5473–5496,doi:10.1175/2007JCLI1824.1, 2007.

Rooney, G. G. and Jones, I. D.: Coupling the 1-D lake model FLake to the community land-surface model JULES, Boreal Env. Res., 15, 501–512, 2010.

Rothman, L. S., Barbe, A., Benner, D. C., Brown, L. R., Camy-Peyret, C., Carleer, M. R., Chance, K., Clerbaux, C., Dana, V., Devi, V. M., Fayt, A., Flaud, J.-M., Gamache, R. R., Goldman, A., Jacquemart, D., Jucks, K. W., Lafferty, W. J., Mandin, J.-Y., Massie, S. T., Nemtchinov, V., Newnham, D. A., Perrin, A., Rinsland, C. P., Schroeder, J., Smith, K. M., Smith, M. A. H., Tang, K., Toth, R. A., Auwera, J. V., Varanasi, P., and Yoshino, K.: The HITRAN molecular spectroscopic database: edition of 2000 including updates through 2001, J. Quant. Spectrosc. Radiat. Transfer, 82, 5–44, doi:10.1016/S0022-4073(03)00146-8, 2003.

Samanta, A., Ganguly, S., Schull, M. A., Shabanov, N. V., Knyazikhin, Y., and Myneni, R. B.: Collection 5 MODIS LAI/FPAR Products, Presented at AGU Fall Meeting, San Francisco, USA, 15–19 December, 2008, 2012.

Scaife, A. A., Butchart, N., Warner, C. D., and Swinbank, R.: Impact of a spectral gravity wave parametrization on the stratosphere in the Met Office Unified Model, J. Atmos. Sci., 59, 1473–1489, doi:10.1175/1520-0469(2002)059<1473:IOASGW>2.0.CO;2, 2002.

Senior, C. A., Arribas, A., Brown, A. R., Cullen, M. J. P., Johns, T. C., Martin, G. M., Milton, S. F., Smith, D. M., Webster, S., and Williams, K. D.: Synergies between numerical weather prediction and general circulation climate models, in: The development of atmospheric general circulation models, edited by: Donner, L., Schubert, W., and Somerville, R., Cambridge University Press, Cambridge, UK, 2010.

Smith, R. N. B.: A scheme for predicting layer cloud and their water content in a general circulation model, Q. J. Roy. Meteorol. Soc., 116, 435–460, doi:10.1002/qj.49711649210, 1990.

Snyder, W. C., Wan, Z., Zhang, Y., and Feng, Y.-Z.: Classification-based emissivity for land surface temperature measurement from space, Int. J. Remote Sens., 19, 2753–2774, doi:10.1080/014311698214497, 1998.

Staniforth, A., Wood, N., and Côté, J.: A simple comparison of four physics-dynamics coupling schemes, Mon. Weather Rev., 130, 3129–3135, doi:10.1175/1520-0493(2002)130<3129:ASCOFP>2.0.CO;2, 2002.

Stirling, A. J. and Stratton, R. A.: Entrainment processes in the diurnal cycle of deep convection over land, Q. J. Roy. Meteorol. Soc., 138, 1135–1149, doi:10.1002/qj.1868, 2012.

Stratton, R. A., Stirling, A., and Derbyshire, S.: Changes and developments to Convective Momentum Transport (CMT) parametrization based on analysis of CRM and SCM, Tech. Rep. 530, Forecsating R&D, Met Office, Exeter, UK, 2009.

Taylor, K. E., Stouffer, R. J., and Meehl, G. A.: A Summary of the CMIP5 Experiment Design, available at: http://cmip-pcmdi.llnl.gov/cmip5/docs/Taylor_CMIP5_design.pdf (last access: 30 November 2013), 2009.

Trigo, I., Freitas, S., Bioucas-Dias, J., Barroso, C., Monteiro, I., and Viterbo, P.: Algorithm Theoretical Basis Document for Land Surface Temperature (LST), Tech. Rep. SAF/LAND/IM/ATBD_LST/1.0, EUMETSAT LSA SAF, 2009.

Tripoli, G. J. and Cotton, W. R.: A numerical investigation of several factors contributing to the observed variable intensity of deep convection over south Florida, J. Appl. Meteorol., 19, 1037–1063, doi:10.1175/1520-0450(1980)019<1037:ANIOSF>2.0.CO;2, 1980.

Untch, A. and Simmons, A. J.: Increased stratospheric resolution in the ECMWF forecasting system, ECMWF Newsletter 82, ECMWF, Reading, UK, 1999.

Uppala, S. M., Kållberg, P. W., Simmons, A. J., Andrae, U., V. Da Costa Bechtold, Fiorino, M., Gibson, J. K., Haseler, J., Hernandez, A., Kelly, G. A., Li, X., Onogi, K., Saarinen, S., Sokka, N., Allan, R. P., Andersson, E., Arpe, K., Balmaseda, M. A., Beljaars, A. C. M., van de Berg, L., Bidlot, J., Bormann, N., Caires, S., Chevallier, F., Dethof, A., Dragosavac, M., Fisher, M., Fuentes, M., Hagemann, S., Hólm, E., Hoskins, B. J., Isaksen, L., Janssen, P. A. E. M., Jenne, R., Mcnally, A. P., Mahfouf, J.-F., Morcrette, J.-J., Rayner, N. A., Saunders, R. W., Simon, P., Sterl, A., Trenberth, K. E., Untch, A., Vasiljevic, D., Viterbo, P., and Woollen, J.: The ERA-40 re-analysis, Quart. J. Roy. Meteorol. Soc., 131, 2961–3012, doi:10.1256/qj.04.176, 2005.

van Genuchten, M. T.: A closed-form equation for predicting the hydraulic conductivity of unsaturated soils, Soil Sci. Soc. Am. J., 44, 892–898, 1980.

Verdin, K. L. and Jensen, S.: Development of continental scale digital elevation models and extraction of hydrographic features, in: Proc. Third Int. Conf. Workshop on Integrating GIS and Environmental Modeling, Santa Barbara, USA, 1996.

Walters, D. N., Best, M. J., Bushell, A. C., Copsey, D., Edwards, J. M., Falloon, P. D., Harris, C. M., Lock, A. P., Manners, J. C., Morcrette, C. J., Roberts, M. J., Stratton, R. A., Webster, S., Wilkinson, J. M., Willett, M. R., Boutle, I. A., Earnshaw, P. D., Hill, P. G., MacLachlan, C., Martin, G. M., Moufouma-Okia, W., Palmer, M. D., Petch, J. C., Rooney, G. G., Scaife, A. A., and Williams, K. D.: The Met Office Unified Model Global Atmosphere 3.0/3.1 and JULES Global Land 3.0/3.1 configurations, Geosci. Model Dev., 4, 919–941, doi:10.5194/gmd-4-919-2011, 2011.

Warner, C. D. and McIntyre, M. E.: An ultrasimple spectral parametrization for nonorographic gravity waves, J. Atmos. Sci., 58, 1837–1857, doi:10.1175/1520-0469(2001)058<1837:AUSPFN>2.0.CO;2, 2001.

Webster, S., Brown, A. R., Cameron, D. R., and Jones, C. P.: Improvements to the representation of orography in the Met Office Unified Model, Q. J. R. Meteorol. Soc., 129, 1989–2010, doi:10.1256/qj.02.133, 2003.

Wells, H., Webster, S., and Brown, A.: The effect of rotation on the pressure drag force produced by flow around long mountain ridges, Q. J. R. Meteorol. Soc., 131, 1321–1338, doi:10.1256/qj.04.37, 2005.

Wentz, F. J. and Spencer, R. W.: SSM/I rain retrievals within a unified all-weather ocean algorithm, J. Atmos. Sci., 55, 1613–1627, note: SSM/I data are produced by Remote Sensing Systems and sponsored by the NASA Earth Science MEaSUREs DISCOVER Project, available at: www.remss.com (last access: 30 November 2013), 1998.

Wilson, D. R. and Ballard, S. P.: A microphysically based precipitation scheme for the UK Meteorological Office Uni-

fied Model, Q. J. R. Meteorol. Soc., 125, 1607–1636, doi:10.1002/qj.49712555707, 1999.

Wilson, D. R., Bushell, A. C., Kerr-Munslow, A. M., Price, J. D., and Morcrette, C. J.: PC2: A prognostic cloud fraction and condensation scheme. I: Scheme description, Q. J. R. Meteorol. Soc., 134, 2093–2107, doi:10.1002/qj.333, 2008a.

Wilson, D. R., Bushell, A. C., Kerr-Munslow, A. M., Price, J. D., Morcrette, C. J., and Bodas-Salcedo, A.: PC2: A prognostic cloud fraction and condensation scheme, II: Climate model simulations, Q. J. R. Meteorol. Soc., 134, 2109–2125, doi:10.1002/qj.332, 2008b.

Wilson, M. F. and Henderson-Sellers, A.: A global archive of land cover and soils data for use in general-circulation climate models, J. Climatol., 5, 119–143,doi:10.1002/joc.3370050202, 1985.

Wood, N., Diamantakis, M., and Staniforth, A.: A monotonically-damping second-order-accurate unconditionally-stable numerical scheme for diffusion, Q. J. R. Meteorol. Soc., 133, 1559–1573, doi:10.1002/qj.116, 2007.

Wood, N., Staniforth, A., White, A., Allen, T., Diamantakis, M., Gross, M., Melvin, T., Smith, C., Vosper, S., Zerroukat, M., and Thuburn, J.: An inherently mass-conserving semi-implicit semi-Lagrangian discretization of the deep-atmosphere global non-hydrostatic equations, Q. J. R. Meteorol. Soc., online first, doi:10.1002/qj.2235, 2013.

Woodward, S.: Mineral dust in HadGEM2, Tech. Rep. 87, Hadley Centre, Met Office, Exeter, UK, 2011.

Xie, P. and Arkin, P. A.: Global precipitation: A 17-year monthly analysis based on gauge observations, satellite estimates, and numerical model outputs, Bull. Am. Meteorol. Soc., 78, 2539–2558, doi:10.1175/1520-0477(1997)078<2539:GPAYMA>2.0.CO;2, 1997.

Zhong, W. and Haigh, J. D.: An efficient and accurate correlated-k parameterization of infrared radiative transfer for troposphere–stratosphere–mesosphere GCMs, Atmos. Sci. Lett., 1, 125–135, doi:10.1006/asle.2000.0022, 2000.

Zhong, W., Osprey, S. M., Gray, L. J., and Haigh, J. D.: Influence of the prescribed solar spectrum on calculations of atmospheric temperature, Geophys. Res. Lett., 35, L22813, doi:10.1029/2008GL035993, 2008.